9164–9177 *Nucleic Acids Research, 2017, Vol. 45, No. 15* *Published online 20 June 2017*
doi: 10.1093/nar/gkx548

CpG and methylation-dependent DNA binding and dynamics of the methylcytosine binding domain 2 protein at the single-molecule level

Hai Pan[1,†], Stephanie M. Bilinovich[2,†], Parminder Kaur[1], Robert Riehn[1], Hong Wang[1,3,*] and David C. Williams, Jr[2,*]

[1]Department of Physics, North Carolina State University, Raleigh, North Carolina, NC 27695, USA, [2]Department of Pathology and Laboratory Medicine, University of North Carolina at Chapel Hill, Chapel Hill, NC 27599, USA and [3]Center for Human Health and the Environment, North Carolina State University, Raleigh, North Carolina, NC 27695, USA

Received April 14, 2017; Revised June 09, 2017; Editorial Decision June 12, 2017; Accepted June 13, 2017

ABSTRACT

The methylcytosine-binding domain 2 (MBD2) protein recruits the nucleosome remodeling and deacetylase complex (NuRD) to methylated DNA to modify chromatin and regulate transcription. Importantly, MBD2 functions within CpG islands that contain 100s to 1000s of potential binding sites. Since NuRD physically rearranges nucleosomes, the dynamic mobility of this complex is directly related to function. In these studies, we use NMR and single-molecule atomic force microscopy and fluorescence imaging to study DNA binding dynamics of MBD2. Single-molecule fluorescence tracking on DNA tightropes containing regions with CpG-rich and CpG-free regions reveals that MBD2 carries out unbiased 1D diffusion on CpG-rich DNA but subdiffusion on CpG-free DNA. In contrast, the protein stably and statically binds to methylated CpG (mCpG) regions. The intrinsically disordered region (IDR) on MBD2 both reduces exchange between mCpG sites along the DNA as well as the dissociation from DNA, acting like an anchor that restricts the dynamic mobility of the MBD domain. Unexpectedly, MBD2 binding to methylated CpGs induces DNA bending that is augmented by the IDR region of the protein. These results suggest that MBD2 targets NuRD to unmethylated or methylated CpG islands where its distinct dynamic binding modes help maintain open or closed chromatin, respectively.

INTRODUCTION

DNA methylation contributes to gene regulation, defines cellular differentiation and genome organization, and therefore plays a diverse role in normal growth and development as well as pathogenesis (1,2). Approximately 1% of nucleotides and 75% of CpG dinucleotides are methylcytosines (3). However, regions of increased CpG content (CpG islands) typically remain unmethylated and often occur in gene promoters (4,5). The methylcytosine-binding domain (MBD) family of proteins selectively bind to methylated CpG sites and modify transcription of the associated gene (6,7). MBD2, a founding member of this family, is a core component of the nucleosome remodeling and deacetylase (NuRD) complex (8). MBD2 localizes the NuRD complex to CpG sites, particularly methylated CpG islands (9,10), and contributes to chromatin remodeling and silencing of the associated gene. The MBD2 protein itself contains three distinct regions, a methylcytosine binding domain (MBD), an intrinsically disordered region (IDR), and a coiled-coil domain. Importantly for the studies reported here, we previously found that the MBD2-IDR both increases binding affinity for DNA and recruits core components of the histone deacetylase sub-complex in NuRD (11).

Unlike most transcription factors, MBD2 functions within the context of CpG islands that contain 100s to 1000s of individual binding sites (5,12). In addition, the NuRD complex contains a chromatin remodeling component that moves nucleosomes along the DNA. Hence, how MBD2 exchanges between binding sites is vital for understanding how methylation-dependent genetic silencing works at a molecular level. Over the past few years, we have been studying how different members of the MBD family bind and distribute on DNA using several NMR-

*To whom correspondence may be addressed. Tel: +1 919 843 9949; Fax: +1 919 966 6718; Email: david_willjr@med.unc.edu
Correspondence may also be addressed to Hong Wang. Tel: +1 919 650 7203; Fax: +1 217 265 0246; Email: hong_wang@ncsu.edu
†These authors contributed equally to this work as first authors.

based techniques, including paramagnetic relaxation enhancement (PRE) (13), residual dipolar coupling measurements (14), chemical shift analyses and N_Z-exchange spectroscopy (14,15). These studies have shown that intra- and intermolecular exchange rates vary between the different MBDs and correlate with their distinct functions. For example, we found that MBD3, a paralogue of MBD2 with low DNA binding affinity, retains an ability to recognize CpG sites and preferentially localize, albeit very weakly, to methylated CpGs. However, MBD3 rapidly exchanges between mCpG specific and non-specific binding modes consistent with the very weak preference for mCpG and a dynamic distribution along the DNA within CpG islands (14). In contrast, MBD2 binds selectively and almost exclusively to a single mCpG when present (14). This observation correlates with whole genome studies that show both MBD2 and MBD3 localize to unmethylated CpG islands while MBD2 more exclusively localizes to methylated CpG islands with silencing of the associated gene (9,10,16,17). In a separate study, we measured intra- and intermolecular exchange between mCpGs by MBD4, an MBD that contains a DNA glycosylase domain involved in mCpG/TpG mismatch repair (15). We found that MBD4 exchanges between methylated sites more rapidly than MBD2. This difference likely reflects a lower binding selectivity for mCpG over CpG and the biological role of MBD4 to rapidly scan methylated CpG regions where mCpG/TpG mismatches occur.

Together, these studies have shown that DNA binding dynamics likely contribute to the specific function of individual MBD proteins. However, the size limitations imposed by NMR restricted the previous studies to relatively small (10–20 base pairs) fragments of DNA. Recently, single-molecule fluorescence techniques have been developed to study transcription factors moving along DNA (18,19). These approaches open the door to studying the dynamic behavior of transcription factors on much larger DNA substrates. In the studies reported here, we correlate our findings on small oligonucleotides with structure and dynamic behavior on much larger, and hence more biologically relevant, fragments of DNA observed using single-molecule fluorescence and atomic force microscopy. These studies lead to several novel observations that help build a model of MBD2 function. We found an unexpected difference in dynamic behavior between CpG-rich and CpG-free regions, in that MBD2 diffuses more rapidly and extensively on CpG-rich sequences than those that lack CpGs (CpG-free). In contrast, MBD2 binds statically or with slow exchange rates when binding to methylated CpG-rich regions. In addition, examining MBD2-DNA complexes by atomic force microscopy shows that binding to CpG-rich sequences leads to marked DNA bending that is further augmented by the IDR when DNA is methylated. Together these studies lead to a model in which MBD2 allows for rapid diffusion and nucleosome remodeling by NuRD within or through CpG rich regions, yet greatly restricts movement and nucleosome remodeling when these islands are methylated. Therefore, the dynamic DNA binding behavior of MBD2 correlates with the biological observation that unmethylated CpG islands are associated with open and transcriptionally active promoters while methylated CpG islands are closed and silenced.

MATERIALS AND METHODS

Protein expression and purification

The chicken $MBD2_{MBD}$ (amino acids 1–71) and human $MBD2_{MBD+IDR}$ (amino acids 150–214) were expressed and purified as previously reported (11,13). Chicken $MBD2_{MBD+IDR}$, which likewise includes an additional 46 residues (amino acids 1–117), was cloned into the previously described pET32a based vector (13), and further modified to replace the thrombin cleave site with a TEV protease cleavage site. The resulting thioredoxin fusion construct was transformed into BL21(DE3) *Escherichia coli* cells grown at 37°C until an OD_{600} of 0.7 and induced with 1 mM IPTG. Bacteria were pelleted and lysed in 20 mM Tris pH 8, 1 M NaCl with sonication. Proteins were further purified via HisTrapFF (GE Life Sciences) and cleaved using either thrombin ($MBD2_{MBD}$) or TEV protease ($MBD2_{MBD+IDR}$). Cleaved proteins were further purified over a Resource-S (GE Life Sciences) ion exchange column and Superdex-75 (GE Life Sciences) using an ÄKTA pure FPLC system (GE Life Sciences). Proteins for NMR analysis were either ^{2}H,^{15}N,^{13}C or ^{2}H,^{15}N labeled. For fluorescence polarization assays the thioredoxin fused protein was purified via HisTrapFF and Superdex-75. For single-molecule experiments $MBD2_{MBD+IDR}$ and $MBD2_{MBD}$ were cloned into pET28a with N-terminal His_6 tags and expressed and purified in a similar manner.

Fluorescence polarization

Protein samples were buffer exchanged into FP buffer [10 mM HEPES pH 7.5, 50 mM NaCl, 3 mM $MgCl_2$, 0.1 mM EDTA, 2 mM DTT and 5% Tween 20]. A 6-FAM labeled 17-bp dsDNA containing a central methylated CpG site (1xmCpG) (14), was annealed and purified by ion exchange chromatography on a Resource Q column (GE Life Sciences). Serial dilutions of the MBD2 protein were added to 10 nM DNA and polarization was measured on a CLARIOstar microplate reader (BMG Labtech) as described previously (11).

NMR spectroscopy

Uniformly H, ^{15}N,^{13}C labeled $MBD2_{MBD+IDR}$ at 0.5 mM bound to methylated DNA was buffer exchanged into 10 mM NaPO4 pH 6.5, 1 mM dithiothreitol, and 10% $^{2}H_2O$. TROSY based version of standard double and triple resonance experiments (HNCOCACB, HNCA, HNCO, HNCACO, HNCACB, ^{15}N-NOESY-HSQC and ^{15}N-HSQC) were collected on a 700 MHz Bruker Avance III spectrometer. Residual dipolar couplings were collected on a ^{2}H,^{13}C,^{15}N labeled sample aligned with 12 mg/ml pf1 bacteriophage (20,21). All data was processed using NMRPipe (22) and analyzed in CcpNMR (23,24).

N_z-exchange spectroscopy

In previous studies, we established that MBD2 shows distinct chemical shifts for several residues when bound to ei-

ther of two dsDNA with a centrally located mCpG. The two sequences differ in the base pairs immediately surrounding the mCpG, which inverts the orientation of bound $MBD2_{MBD}$ (WT: 5′-GGAT(**^{m}C**)GGCTCCTC-3′; INV: 5′-GGAC(**^{m}C**)GACTC-3′) (13,15). A 350 μM sample of $^{2}H,^{15}N$ labeled $MBD2_{MBD}$ was incubated with 275 μM WT DNA and 275 μM INV DNA (yielding 175 μM of each complex with 100 μM excess of each DNA). Samples with 200 and 300 μM excess DNA were collected by adding a 1.25 mM mixture of WT and INV DNA. For each titration point a series of 2D-^{15}N TROSY N_z-exchange spectra were obtained with the following delays: 11.9, 14.3, 16.8, 21.8, 29.3, 36.8, 49.3, 61.8, 118.9 and 211.8 ms. Two samples of $MBD2_{MBD+IDR}$ were prepared: one with 370 μM of $MBD2_{MBD+IDR}$ and 285 μM of each DNA (yielding 185 μM of each complex with 100 μM excess of each DNA) and a sample with 370 μM protein with 740 μM of each DNA (185 μM of each complex with 555 μM excess of each DNA). 2D-^{15}N TROSY N_z-exchange spectra (25) were collected and processes as described previously (15).

DNA substrates for single-molecule imaging

To generate a DNA substrate incorporating a known target sequence for MBD2 (26), we subcloned a portion (3837 base pairs) of the death associated protein kinase 1 (DAPK1) promoter (chromosome 9, bases 87497573 to 87501409) which includes CpG-rich (4689 base pair) and CpG-poor (2150 base pairs) regions. This sequence was then further sub-divided into clones that contain only the CpG-rich region (CpG-rich: 4705 bp) or rich plus poor regions to generate the CpG-rich-poor DNA (6839 bp) within the pGEM backbone (Supplementary Figure S2). For a CpG-free DNA substrate, the pCpGfree-vitroNmcs plasmid (5488 base pairs) was purchased from InvivoGen that is devoid of any CpG dinucleotides. The CpG-rich region from the DAPK1 promoter was then sub-cloned into the ScaI/NcoI restriction sites to generate a 1697 base pair CpG-rich region within a 5466 CpG-free backbone (CpG-free-rich DNA: 7163 bp).

For DNA methylation, purified plasmids were treated with CpG Methyltransferase (M.SssI) and S-Adenosine methionine (SAM) as a cofactor at 37°C for overnight. The methylation status of the DNA was confirmed by restriction digestion using HpaII. A total of 42 HpaII sites are present in both the CpG-rich and CpG-rich-poor substrates. Among these, 30 sites are in the CpG-rich region on the CpG-rich and CpG-rich-poor DNA substrates. To generate longer DNA substrates for the DNA tightrope assay, linearized DNA substrates were ligated using the Quick Ligation™ Kit (New England BioLabs) at room temperature for overnight. Ligated DNA samples were then purified using phenol-chloroform extraction.

Protein-QD conjugation

Streptavidin-conjugated quantum dots (SAv-QDs-655) were purchased from Invitrogen. For QD labeling of N-terminal His_6-tagged MBD2 (His-$MBD2_{MBD}$ and His-$MBD2_{MBD+IDR}$), 1 μl of SAv-QDs-655 (1 μM) was incubated with 1 μl of the multivalent chelator tris-nitrilotriacetic acid (^{BT}tris-NTA, 2 μM) for 20 min at room temperature (27). The His-MBD2 protein (1 μl of 1 μM) was then added to the SAv-QD-NTA solution and incubated for an additional 20 min at room temperature. All samples were diluted 100X before being introduced into the flow cell in the imaging buffer (50 mM HEPES pH 7.5, 100 mM NaCl, and 1 mM $MgCl_2$).

Fluorescence imaging and analysis

The oblique angle total internal reflection microscopy based particle tracking of QD-labeled proteins on DNA tightropes was described previously (28). Briefly, an inverted microscope (Nikon Ti-E) and a 100× objective (APO TIRF, Nikon) was used in the experiments. Red (655 nm) QD-protein complexes were excited at 488 nm by a solid-state laser (Sapphire DPSS). The signal was split into two channels using a dichroic mirror (T605LPXR, Chroma) and an emission filter (ET655/40nm, Chroma). Flow cells were assembled as methods demonstrated in preceding studies (28). Furthermore, we immobilized poly-L-lysine (2.5 mg/ml, M.W. >300 kDa, Wako Chemicals) treated silica beads onto a cover slip surface with PEGlyation, and then introduced ligated DNA substrates into the flow cell with a syringe pump at a flow rate of 300 μl/min. All images were taken using an EMCCD (iXon DU897, Andor Technology) at a time resolution of 50 ms/frame.

The mean square displacement (MSD) as a function of time interval is given by:

$$\mathrm{MSD}(n\Delta t) = \frac{1}{N-n}\sum_{i=1}^{N-n}[(x_{i+n}-x_i)^2] \qquad (1)$$

where N is the total number of frames in the trajectory, n is the number of frames for different time intervals, Δt is the time between frames and x_i is the position of the protein-QD in the frame i. The 1D diffusion constant (D) and diffusion exponent (alpha factor) were analyzed by a custom routine developed in LabView Software based on the following equation (29):

$$\mathrm{MSD} = 2Dt^{\alpha} \qquad (2)$$

A protein was categorized as being mobile if the diffusion constant was greater than 1×10^{-5} μm^2/s and the R^2 value from data fitting using Equation (2) was >0.8. The diffusion range was analyzed using a custom code written using MATLAB.

AFM imaging and image analysis

All DNA and protein samples were pre-incubated for 20 min at room temperature and diluted 10-fold in 1× AFM buffer [25 mM NaOAc, 25 mM HEPES–KOH (pH 7.5) and 10 mM $Mg(OAc)_2$] before being deposited onto a freshly cleaved mica (SPI Supply). The samples were then washed with MilliQ water and dried with nitrogen gas. The final concentration of DNA substrates on mica was ∼0.5 ng/μl and of protein was 30 nM. All images were obtained in the AC mode using a MFP-3D-Bio AFM (Asylum Research). Cantilevers (PPP-FMR, Nanosensors) with spring constants at ∼2.8 N/m were used. The images were collected at the scan size of 3 μm × 3 μm, scan rate of 1–2

Hz, and resolution of 512 × 512 pixels. The DNA bending angle was analyzed using either the Asylum software or a custom MATLAB code, which provide similar results. The MATLAB code determines the center of the DNA-bound protein by performing a 2D Gaussian fit in the vicinity of the highest point of the complex, followed by a sampling of the height along a circle around that point. The angle between the intersection points of DNA and sampling circle was determined by local Gaussian fitting in the vicinity of the two height maxima.

RESULTS

The IDR of MBD2 influences DNA binding affinity

We previously found that a short, positively charged region just C-terminal to the human MBD2 (MBD) augments binding affinity for methylated DNA by 10–100-fold (11). In the current work, we studied the chicken orthologue (96%, 94%, and 83% identical to human $MBD2_{MBD}$, $MBD2_{MBD+IDR}$, and MBD2b, respectively) for which we have a high-resolution solution structure and NMR assignments (13). Of note, the human MBD2a isoform includes a long unstructured N-terminal glycine–arginine repeat region that likely increases DNA binding affinity and unique binding interactions (30). Yet, the MBD2b isoform can compact chromatin and functionally replace MBD2a (10). Fluorescence polarization binding analysis shows that the homologous region (IDR) increases binding affinity of the chicken MBD2 by ∼12-fold (Supplementary Figure S1A). In addition, we measured residual dipolar couplings (RDC) for $MBD2_{MBD+IDR}$ bound to methylated DNA and fit them to the known structure of the isolated domain (13). The overall quality of fit (Q factor = 47%) and correlation between measured and predicted structure ($r = 0.85$) indicate that the IDR does not significantly alter the fold of the MBD (Supplementary Figure S1B and C). As we demonstrated previously, though, both the lack of chemical shift dispersion and RDC measurements indicate that the IDR does not adopt a regular structure when bound to DNA.

In previous studies of MBD proteins, we have consistently found that the ^{1}H–^{15}N chemical shifts for backbone (G27 and A30) and side chain (R24) resonances of three highly conserved residues reflect the distribution between methylation specific and non-specific binding modes (14,15,31). Hence, the location of these resonances reflects the amount of time spent bound to the methylated site. Comparing the chemical shifts for these reporter residues between $MBD2_{MBD+IDR}$ and $MBD2_{MBD}$ (Figure 1A and B) shows that the IDR does not alter the relative distribution of MBD2 between binding modes. Likewise, the largest chemical shift differences (Figure 1C) map to the C-terminal portion of the MBD, just prior to the additional amino acid sequence unique to the $MBD2_{MBD+IDR}$ clone. Therefore, the increase in binding affinity provided by the IDR does not change the structural recognition of mCpG or methylation selectivity of the protein.

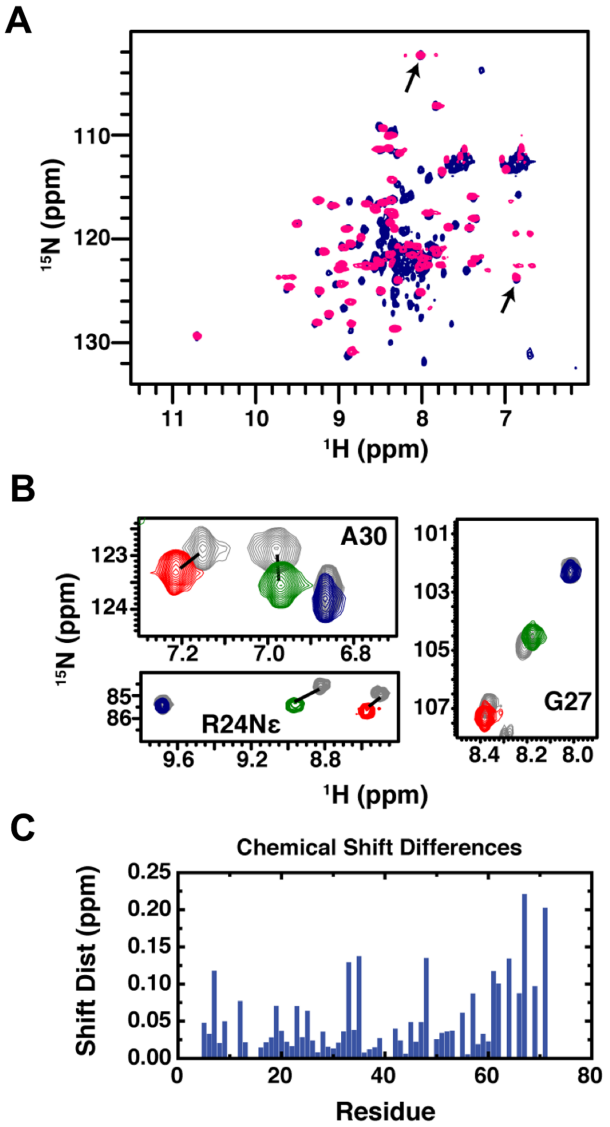

Figure 1. Comparison of NMR chemical shifts between $MBD2_{MBD+IDR}$ and $MBD2_{MBD}$ bound to DNA. (**A**) An overlay of 2D ^{15}N-HSQC spectra for $MBD2_{MBD+IDR}$ (navy) and $MBD2_{MBD}$ (pink) bound to mCpG DNA reveals very similar chemical shifts for most amide resonances including those for reporter resonances G27 and A30 (arrows). (**B**) Expanded regions from 2D ^{15}N-HSQC spectra for $MBD2_{MBD+IDR}$ bound to DNA without CpG dinucleotides (red), with 3 CpG dinucleotides (green) and 1 mCpG dinucleotide (navy) are shown for reporter residues A30, R24 Nε, and G27. For comparison, the same regions are shown for $MBD2_{MBD}$ (gray) bound to the same DNA with equivalent resonances connected by lines (if they do not overlap). (**C**) The chemical shift distances between $MBD2_{MBD+IDR}$ and $MBD2_{MBD}$ backbone amide resonances shows relatively small changes for most residues, with some of the larger differences immediately preceding the additional residues in $MBD2_{MBD+IDR}$.

$MBD2_{MBD+IDR}$ and $MBD2_{MBD}$ carry out unbiased 1D diffusion on CpG-rich DNA and subdiffusion on CpG-free DNA

Dynamic movements of proteins on DNA, such as 1D sliding, jumping, and hopping are essential for a protein to find its targeted sequences or structures on DNA (18,32–36). Furthermore, the MBD2–NuRD complex rearranges nucleosomes within the context of large CpG islands and mod-

ifies higher order chromatin organization (37,38). Therefore, to further understand how MBD2 dynamically distributes on much larger DNA substrates and the role of the IDR, we applied oblique angle total internal reflection fluorescence (OAF) microscopy imaging of quantum dot (QD)-labeled proteins (28,39–41). We tested MBD2 with ($MBD2_{MBD+IDR}$) or without ($MBD2_{MBD}$) a portion of the IDR on DNA tightropes with or without CpG sequences (Materials and Methods, Figure 2A). The CpG-rich and CpG-poor regions contain 6.5–9.5 and 0.6 CpG sites per 100 bp DNA, respectively (Supplementary Figure S2). The DNA substrates used for the DNA tightrope assay were generated by ligating linear DNA fragments containing unmethylated CpG-rich, CpG-free plus rich (CpG-free-rich), CpG-free (CpG-free), or CpG-rich plus poor (CpG-rich-poor) sequences (Figure 2 and Supplementary Figure S2). Both fluorescence imaging of YOYO1-stained ligated DNA and AFM imaging of unstained ligated DNA demonstrated the formation of longer DNA fragments after ligation (Supplementary Figure S3 A,B). We conjugated His-tagged $MBD2_{MBD+IDR}$ and $MBD2_{MBD}$ to streptavidin-coated quantum dots (SAv-QDs) through the multivalent chelator tris-nitrilotriacetic acid (^{BT}tris-NTA) linker (27) (Figure 2B). The three Ni-NTA moieties on the circular scaffold of the tris-NTA adaptor bind the His-tag with subnanomolar affinity (27,42). AFM and fluorescence imaging established that SAv-QDs without MBD2 did not have significant binding affinity for DNA. Hydrodynamic flow was used to stretch DNA and suspend ligated DNA strands between poly-L-lysine coated silica microspheres at an elongation of ∼90% of the DNA contour length (Figure 2C) (28). Following formation of the DNA tightropes, either QD-labeled $MBD2_{MBD+IDR}$ or $MBD2_{MBD}$ was introduced into the flow cell. The binding of MBD2-QDs molecules to DNA tightropes was long lived, with ∼99% of the $MBD2_{MBD+IDR}$ and $MBD2_{MBD}$ binding on the DNA tightropes throughout the observation window (2 min, $N = 257$ for $MBD2_{MBD+IDR}$ and $N = 254$ for $MBD2_{MBD}$). Analysis of MBD2 on DNA tightropes revealed two populations (Table 1): static and mobile molecules. Overall, on the unmethylated DNA tightropes, the majority of $MBD2_{MBD+IDR}$ and $MBD2_{MBD}$ molecules are mobile (>65%, Table 1).

To obtain diffusion constants for mobile $MBD2_{MBD+IDR}$ and $MBD2_{MBD}$ on DNA tightropes, the position of $MBD2_{MBD+IDR}$- and $MBD2_{MBD}$-QDs on DNA was tracked by Gaussian fitting to kymographs (particle position versus time plots, Figure 2D) (39,41). Diffusion constants and diffusive exponents (alpha factors) were obtained from fitting the MSD versus time plots (Figure 3A and B). An alpha exponent of 1 indicates an unbiased random walk and a value <1 indicates subdiffusion (29). At the same protein concentrations (10 nM in the flow cell), the diffusion constants of $MBD2_{MBD+IDR}$ and $MBD2_{MBD}$ on CpG-rich and CpG-free-rich substrates were indistinguishable (Figure 3C and Table 2). However, the diffusion constants displayed by $MBD2_{MBD+IDR}$ and $MBD2_{MBD}$ on the CpG-free DNA tightrope were significantly slower compared to those on DNA tightropes containing CpG sequences (CpG-rich and CpG-free-rich) (Figure 3C).

In addition, on the CpG-rich tightropes $MBD2_{MBD+IDR}$ and $MBD2_{MBD}$ displayed similar alpha exponents that are close to 1 (0.95 ± 0.03 and 0.92 ± 0.02, respectively), indicating unbiased 1D diffusion on DNA (Figure 3D, Table 2). Surprisingly, inclusion of CpG-free sequences in the DNA tightropes significantly ($P < 0.05$) reduced the alpha exponents for both $MBD2_{MBD+IDR}$ and $MBD2_{MBD}$ (Figure 3D, Table 2), indicating subdiffusive motion. Overall, both $MBD2_{MBD+IDR}$ and $MBD2_{MBD}$ display significantly ($P<0.005$) narrower diffusion ranges on the CpG-free DNA tightropes compared to all the other DNA tightropes containing CpG-rich sequences (CpG-rich and CpG-free-rich, Supplementary Figure S4). In summary, fluorescence imaging shows that the IDR does not significantly modify the 1D diffusion of MBD2 on DNA. However, both $MBD2_{MBD+IDR}$ and $MBD2_{MBD}$ show unbiased diffusion on CpG-rich DNA while subdiffusive motion on CpG-free sequences.

Both $MBD2_{MBD}$ and $MBD2_{MBD+IDR}$ become static on methylated DNA

To evaluate how DNA methylation affects the dynamics of MBD2 on DNA, we imaged QD-labeled $MBD2_{MBD+IDR}$ and $MBD2_{MBD}$ on the CpG-free-rich (Figure 4), CpG-rich, and CpG-rich-poor (Supplementary Figures S5 and S6) DNA tightropes after methylation. Linear DNA substrates were methylated before ligation using CpG Methyltransferase (M.SssI) with S-Adenosine methionine (SAM) as a cofactor (Supplementary Figure S3C). The methylation status of the linear DNA substrates was confirmed by inhibition of digestion by HpaII restriction enzyme (Supplementary Figure S3C). When methylated, the CpG-rich, CpG-free-rich, and CpG-poor-rich DNA contain 42, 30 and 42 HpaII restriction sites, respectively. Importantly, lack of methylation of just one site permits cleavage of the vector by the enzyme. Hence, absence of digestion indicates a high level of methylation (43). We then ligated the methylated DNA and used hydrodynamic flow to form DNA tightropes between silica beads inside the flow cell. AFM imaging showed that QD-labeled $MBD2_{MBD+IDR}$ retains binding specificity for mCpG-rich region on the linear mCpG-free-rich DNA (Supplementary Figure S5). As compared to unmethylated DNA, the binding events for both $MBD2_{MBD+IDR}$ and $MBD2_{MBD}$ increased dramatically on methylated DNA tightropes (Supplementary Figure S6A,B). Combining the data for all three DNA substrates (CpG-rich, CpG-rich-poor, and CpG-free-rich), the density of both $MBD2_{MBD+IDR}$ and $MBD2_{MBD}$ complexes increased from 1.5/40 kb on unmethylated DNA to 4/40 kb on methylated DNA (Supplementary Figure S6C and D). Similar to what was observed on the unmethylated DNA, the binding of MBD2-QDs molecules to methylated DNA was long lived, with over 99% of the $MBD2_{MBD+IDR}$ and $MBD2_{MBD}$ binding on the DNA tightropes throughout the observation window (2 min, $N = 518$ for $MBD2_{MBD+IDR}$ and $N = 445$ for $MBD2_{MBD}$). However, in contrast to the unmethylated DNA tightropes, the majority (∼91.2% to 95.5%) of the $MBD2_{MBD+IDR}$ and $MBD2_{MBD}$ bound statically to the methylated DNA tightropes (Figure 4, Supplementary Figure S6, and Table 1). Furthermore, the dis-

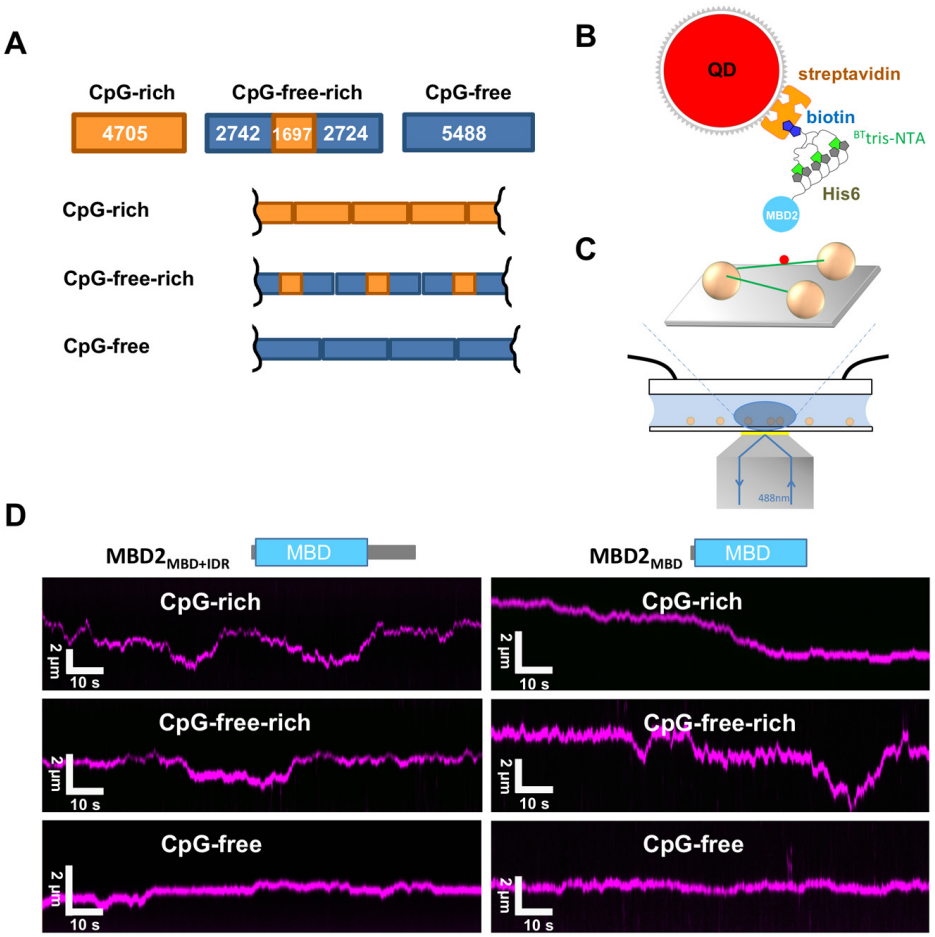

Figure 2. $MBD2_{MBD+IDR}$ and $MBD2_{MBD}$ carry out 1D diffusion on tightropes with or without unmethylated-CpG sequences. (**A**) Cartoon drawing of three ligated DNA substrates for the DNA tightrope assay: CpG-rich, CpG-free-rich and CpG-free. The numbers in the boxes show the length of the DNA. (**B**) Schematic representation of QD-conjugated $MBD2_{MBD+IDR}$ and $MBD2_{MBD}$ using ^{BT}tris-NTA as the linker between the His_6-tag on the MBD2 proteins and streptavidin coated-QD. (**C**) Schematic drawing of the DNA tightrope assay depicting a QD-labeled protein (red dot) on the DNA tightrope (green lines) stretched between silica beads (golden spheres) immobilized on a passivated glass surface. (**D**) Representative kymographs of red (655 nm) QD-labeled $MBD2_{MBD+IDR}$ (left panel) and $MBD2_{MBD}$ (right panel) on three different DNA tightropes.

Table 1. Proportion of static MBD2 on unmethylated- and methylated-DNA tightropes

DNA		$MBD2_{MBD+IDR}$		$MBD2_{MBD}$	
		Percentage (%)	*N*	Percentage (%)	*N*
Unmethylated	CpG-rich	32.1% ± 4.9%	74	33.8% ± 5.2%	91
	CpG-free-rich	22.7% ± 2.3%	127	22.9% ± 1.2%	95
	CpG-free	10.6% ± 3.9%	69	15.7% ± 3.7%	56
Methylated	CpG-rich	91.2% ± 2.3%	284	93.6% ± 2.2%	173
	CpG-free-rich	94.8% ± 1.8%	234	95.5% ± 1.3%	272
	CpG-free	N.A.		N.A.	

The values represent mean ± SEM from two to three experiments for each data set.

Table 2. Diffusion of $MBD2_{MBD+IDR}$ and $MBD2_{MBD}$ on three DNA substrates

DNA	$MBD2_{MBD+IDR}$			$MBD2_{MBD}$		
	D ($\mu m^2/s$)	α exponent	*N*	D ($\mu m^2/s$)	α exponent	*N*
CpG-rich	0.089 ± 0.016	0.95 ± 0.03	44	0.078 ± 0.012	0.92 ± 0.02	59
CpG-free-rich	0.071 ± 0.013	0.75 ± 0.02	93	0.057 ± 0.013	0.81 ± 0.03	73
CpG-free	0.014 ± 0.003	0.79 ± 0.02	90	0.019 ± 0.003	0.82 ± 0.03	88

The values represent mean ± SD from 2 to 5 experiments for each data set.

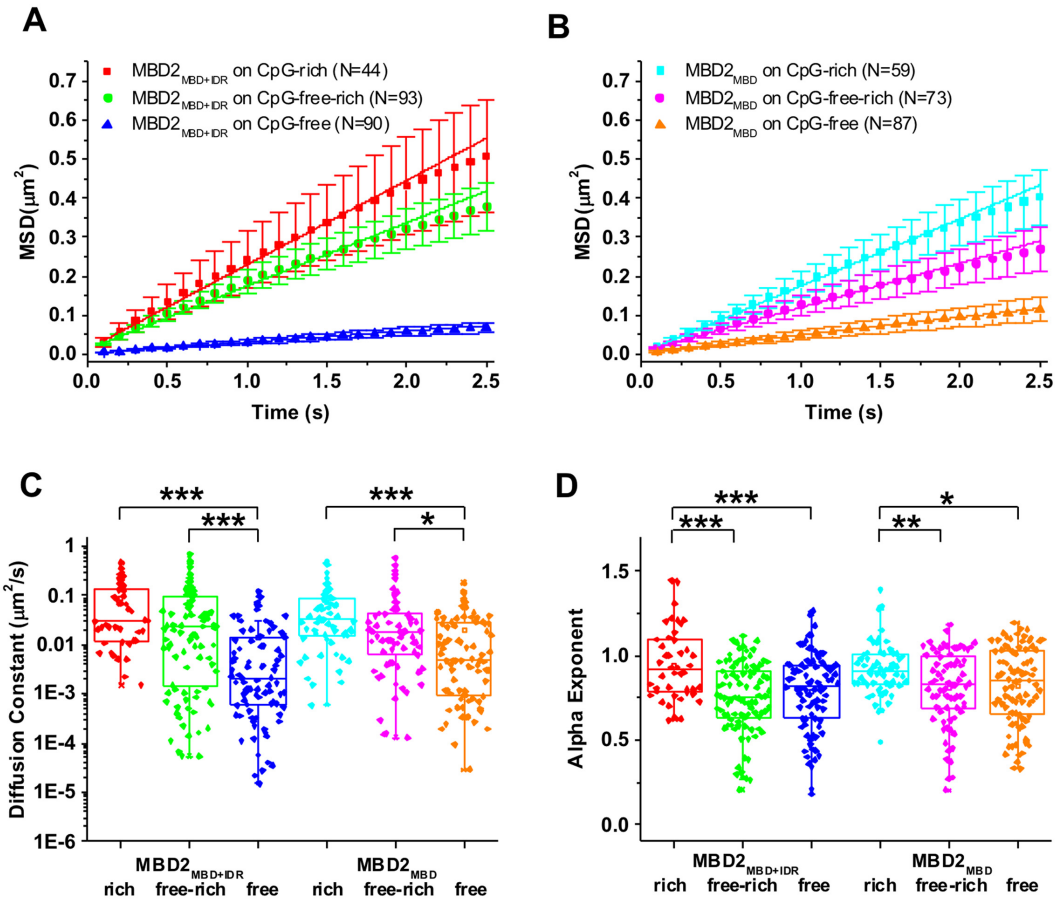

Figure 3. Diffusion constant, alpha exponent of $MBD2_{MBD+IDR}$ and $MBD2_{MBD}$ on three types of DNA substrates. Plots of average values of MSD versus time for $MBD2_{MBD+IDR}$ (**A**) and $MBD2_{MBD}$ (**B**) on CpG-rich, CpG-free-rich and CpG-free DNA tightropes. The error bars represent SEM. (**C** and **D**) Diffusion constants (**C**) and alpha exponents (**D**) of $MBD2_{MBD+IDR}$ and $MBD2_{MBD}$ on CpG-rich, CpG-free-rich, and CpG-free DNA tightropes (Table 2). ***$P < 0.0005$; **$P < 0.005$; *$P < 0.5$.

tance between adjacent proteins on the methylated CpG-free-rich DNA tightropes are Gaussian distributed with peaks centered at 2.33 (± 0.38) μm and 4.19 (± 0.65) μm for $MBD2_{MBD+IDR}$, and 2.15 (± 0.39) μm and 4.15 (± 0.37) μm for $MBD2_{MBD}$, respectively (Figure 4B and C). These spacing match the distances between methylated CpG-rich regions on DNA tightropes (Figure 4A). Taken together, fluorescence imaging of $MBD2_{MBD+IDR}$ and $MBD2_{MBD}$ on DNA tightropes establishes that MBD2 recognizes methylated CpG sites through stable and static binding.

Intra- and intermolecular exchange by MBD2

While the single-molecule studies clearly demonstrate that methylation greatly restricts dynamic mobility of MBD2 on DNA, the spatial resolution (~16 nm) of fluorescence imaging limits localization accuracy of the MBD2 protein to ~50 base pairs of DNA (28), which contains ~5 CpG dinucleotides based on the density of the CpG sites (Supplementary Figure S2). In previous studies, we found that the MBD can exchange relatively rapidly between closely-spaced mCpG sites (10–20 base pair separation) on the same DNA (intramolecular exchange, lifetimes <1 ms) and between different molecules of DNA (intermolecular exchange, lifetimes of 20–30 ms) (15). Hence, to test whether the IDR modifies local exchange between individual methylated sites, we compared intra- and intermolecular exchange for $MBD2_{MBD+IDR}$ and $MBD2_{MBD}$. Several resonances in the 2D ^{15}N-HSQC spectrum of MBD2 show different chemical shifts when bound to closely related 10 base pair oligonucleotides that differ in sequence immediately adjacent to the central mCpG dinucleotide (WT and INV, Figure 5A and B). When $MBD2_{MBD+IDR}$ is bound to a 20-base pair fusion of these two sequences, with the mCpGs separated by only 10 bases, the 2D ^{15}N-HSQC spectrum contains two separate peaks consistent with slow exchange between the binding sites (Figure 5B middle panel). In contrast, when $MBD2_{MBD}$ is bound to the same sequence, the spectrum contains only a single broadened peak at the average position between the two resonances (Figure 5B bottom panel). Hence, the IDR decreases the rate of intramolecular exchange from fast to slow exchange on the NMR timescale.

To determine whether the IDR influences intermolecular exchange, we used N_z exchange spectroscopy to measure the intermolecular exchange rate between the WT and INV methylated CpG sequences, as we have described previously (15). We followed the auto and exchange cross peaks as a function of N_Z delay, and fit the intensities to four cou-

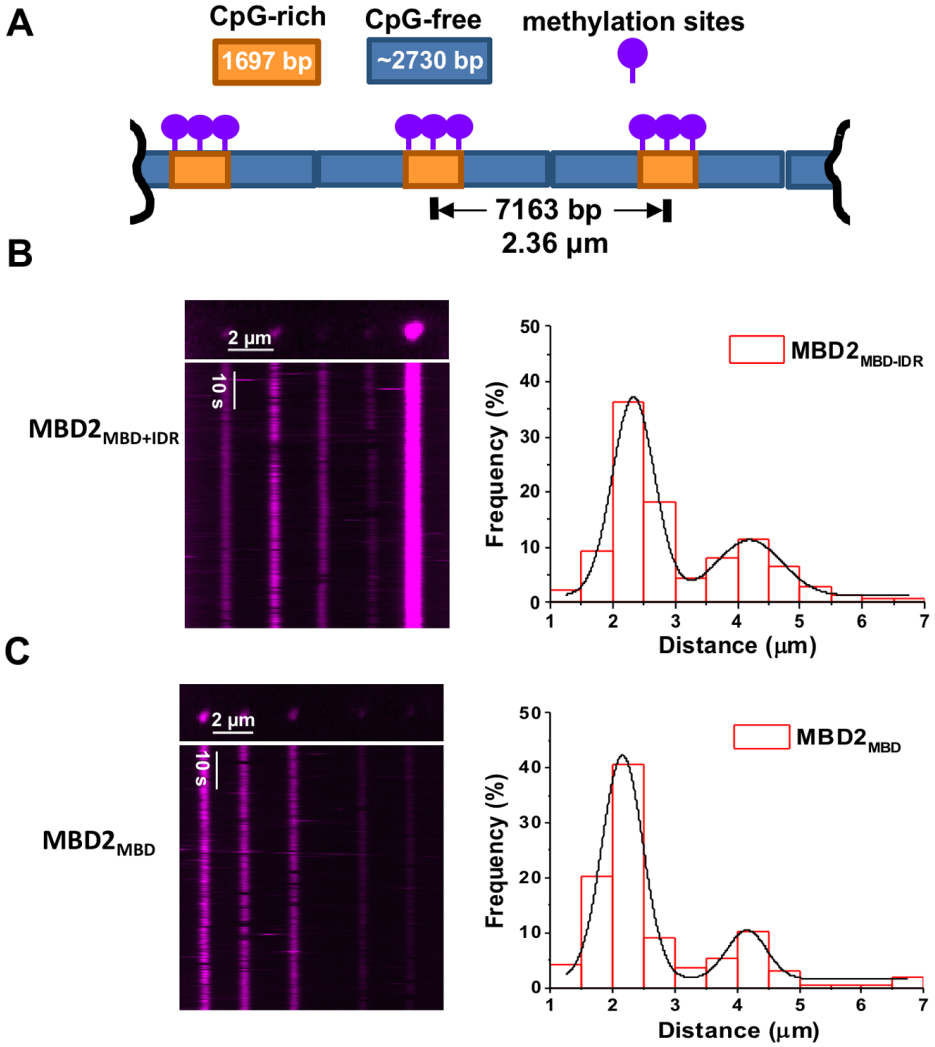

Figure 4. Both $MBD2_{MBD+IDR}$ and $MBD2_{MBD}$ become static at the methylated CpG-rich regions on DNA tightropes. (**A**) A cartoon drawing of the ligated DNA substrates containing alternating mCpG-rich and CpG-free sequences (mCpG-free-rich) for the DNA tightrope assay. The DNA is methylated using CpG Methyltransferase (M.SssI) and S-Adenosine methionine (SAM) as a cofactor. The expected center-to-center distance between two nearest neighbor CpG-rich regions on DNA tightropes is 2.1 μm, assuming 90% extension of the DNA contour length. QD-labeled $MBD2_{MBD+IDR}$ (**B**) and $MBD2_{MBD}$ (**C**) on the ligated mCpG-free-rich DNA tightropes. Left panels: Fluorescence images (top) and corresponding kymographs (bottom). Right panels: histograms of the distance between two adjacent $MBD2_{MBD+IDR}$ (B) and $MBD2_{MBD}$ (C) on mCpG-free-rich DNA tightropes. The solid lines represent double Gaussian fits to the data ($R^2 > 0.98$) with peaks centered at 2.33 (±0.38) μm and 4.19 (±0.65) μm for $MBD2_{MBD+IDR}$ ($N = 138$), and 2.15 (±0.39) μm and 4.15 (±0.37) μm for $MBD2_{MBD}$ ($N = 167$), respectively.

pled equations describing molecular exchange in the slow limit (44). We measured very similar exchange rates for both $MBD2_{MBD+IDR}$ and $MBD2_{MBD}$ with 100 μM excess DNA (Figure 5C and D). However, increasing the excess DNA concentration enhanced the exchange rates for $MBD2_{MBD}$ but not for $MBD2_{MBD+IDR}$ (Figure 5C–E). Without the IDR, the strong free DNA concentration dependence for $MBD2_{MBD}$ indicates that intermolecular exchange is rate limited by the DNA re-binding on-rate or intersegment transfer (45,46). In contrast, in the presence of the IDR, the lack of free DNA concentration dependence indicates that DNA dissociation is rate limiting for $MBD2_{MBD+IDR}$ (45,46). Therefore, the IDR both reduces exchange between mCpG sites along the DNA as well as dissociation from DNA, acting like an anchor that restricts dynamic mobility of the MBD domain.

MBD2 bends DNA and IDR augments the bending upon binding to mCpG

In order to evaluate whether MBD2 with or without the IDR affects the DNA conformation upon binding, we applied AFM imaging in air to visualize the $MBD2_{MBD+IDR}$- and $MBD2_{MBD}$-DNA complexes on linear CpG-free DNA (Figure 6), as well as unmethylated and methylated CpG-rich DNA (Figure 7). Due to its small size, it is challenging to unambiguously identify $MBD2_{MBD+IDR}$ (138 amino acids) and $MBD2_{MBD}$ (91 amino acids) on DNA in topographical AFM images. To increase the size of $MBD2_{MBD+IDR}$ and $MBD2_{MBD}$ and facilitate visualization,

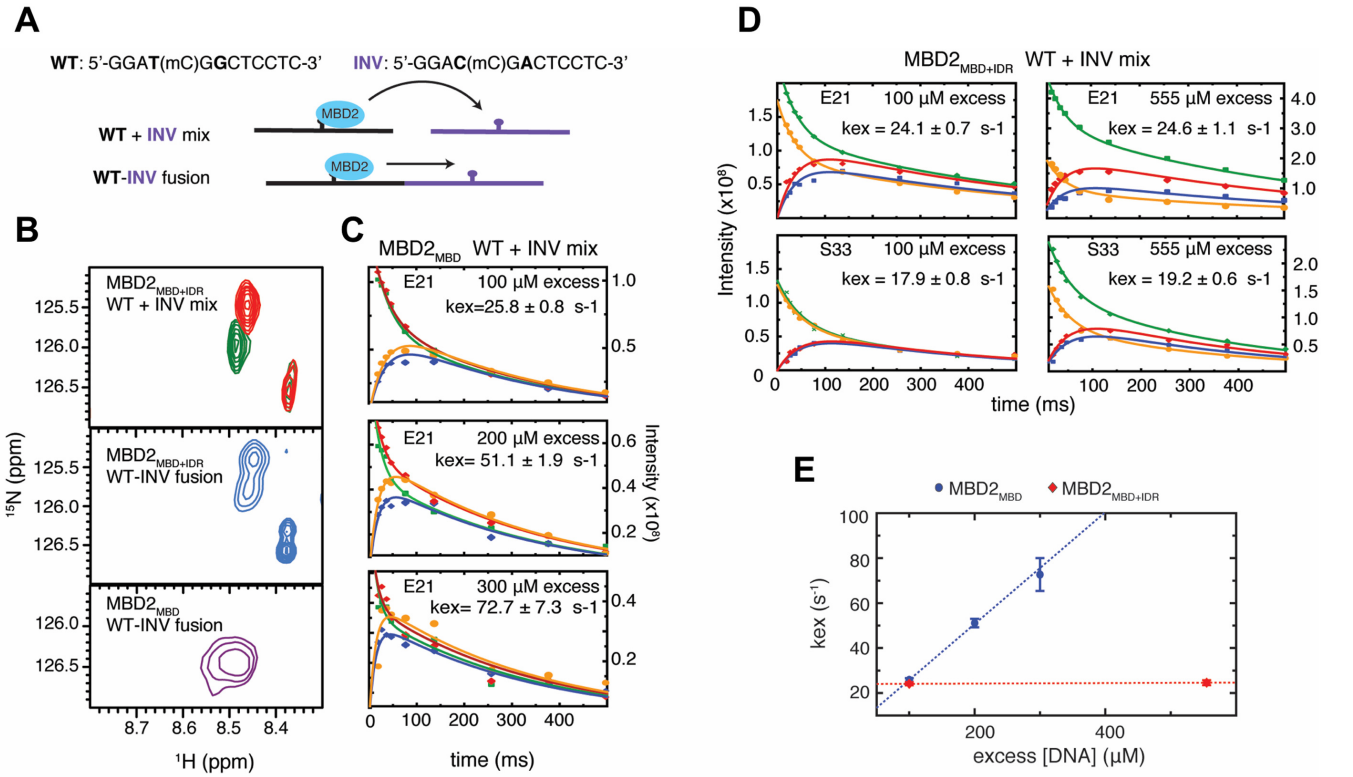

Figure 5. The MBD2 IDR influences both intramolecular between mCpG sites and intermolecular exchange between different DNA molecules. (**A**) Sequence of WT and INV DNA with a central methylated CpG. The two base pairs that differ between the two sequences (bold) lead to unique chemical shifts in the bound state. MBD2 was bound to a mixture or fusion of the WT and INV sequences for inter- and intra-molecular exchange rate measurements, respectively. (**B**) An overlay of 2D ^{15}N-HSQC spectra for $MBD2_{MBD+IDR}$ bound to a mixture of WT and INV DNA (top panel), $MBD2_{MBD+IDR}$ and $MBD2_{MBD}$ bound to the fusion of WT and INV DNA (middle and bottom panels, respectively). (**C**) N_Z exchange curves for $MBD2_{MBD}$ residue E21 bound to a mixture of WT and INV DNA with 100 μM, 200 μM, and 300 μM excess free DNA. (**D**) N_Z exchange curves for $MBD2_{MBD+IDR}$ residues E21 and S33 bound to 100 μM and 555 μM excess free DNA. (**E**) Plot of the measured intermolecular exchange rates versus excess DNA concentration.

the thioredoxin (TRX) tag was not removed from the N-termini of the proteins. Importantly, the TRX tag does not significantly modify methylated DNA binding affinity (Supplementary Figure S1). Representative images of CpG-free only (Figure 6A), as well as TRX-$MBD2_{MBD+IDR}$ and TRX-$MBD2_{MBD}$ on linear CpG-free DNA substrates (Figure 6B) show examples of DNA only and the protein–DNA complexes. The heights of TRX-$MBD2_{MBD+IDR}$ and TRX-$MBD2_{MBD}$ on DNA (0.49 ± 0.06 nm and 0.45 ± 0.06 nm, respectively) were significantly ($P < 0.00001$) taller than that of dsDNA itself (0.29 ± 0.04 nm) allowing us to unambiguously identify the protein-DNA complexes (Figure 6B). A striking feature from these images is the DNA bending induced by both proteins on CpG-free (Figure 6), as well as CpG-rich, and mCpG-rich DNA (Figure 7). As compared to DNA alone, $MBD2_{MBD+IDR}$ and $MBD2_{MBD}$ induced a small degree of DNA bending on CpG-free DNA (36.7°±27.6° and 39.2°±13.7°, respectively, Table 3). The DNA bending angles induced by $MBD2_{MBD+IDR}$ and $MBD2_{MBD}$ on CpG-rich DNA (66.4° ± 32.4° and 68.8°± 30.7°, respectively) were larger than observed for CpG-free, but still comparable between the two proteins (Table 3). In contrast, $MBD2_{MBD+IDR}$ induced significantly ($P < 1 \times 10^{-6}$) larger bending angles on methylated CpG-rich (103.5° ± 23.1°) DNA, while $MBD2_{MBD}$ did not (69.0°± 32.6°, Table 3).

To rule out the possibility that sample variation contributed to these differences in DNA bending, we analyzed $MBD2_{MBD+IDR}$- and $MBD2_{MBD}$-induced DNA bending angles on the CpG-free and CpG-rich regions present in the same linear DNA (unmethylated and methylated CpG-free-rich DNA substrates, Supplementary Figures S7 and S8). Even though we could not differentiate the two DNA ends from each other, the central location of the CpG-rich region on the linear DNA substrate (38% to 62% measured from either end) allowed us to assign the MBD2 binding to either the CpG-free or CpG-rich regions (Supplementary Figures S7C and S8C). Analysis of the binding position of $MBD2_{MBD+IDR}$ and $MBD2_{MBD}$ on the unmethylated and methylated CpG-free-rich DNA showed that both $MBD2_{MBD+IDR}$ and $MBD2_{MBD}$ preferentially bound to the CpG-rich region (Supplementary Figures S7C and S8C). Bending angle analysis on the CpG-free-rich DNA substrates confirmed the results from using DNA substrates of CpG-free (Figure 6) and CpG-rich only sequences (Figure 7). On the linear unmethylated CpG-free-rich DNA, both $MBD2_{MBD+IDR}$ and $MBD2_{MBD}$ induced additional bending on the CpG-rich region as compared to at the CpG-free region (Supplementary Figure S7). Importantly, while

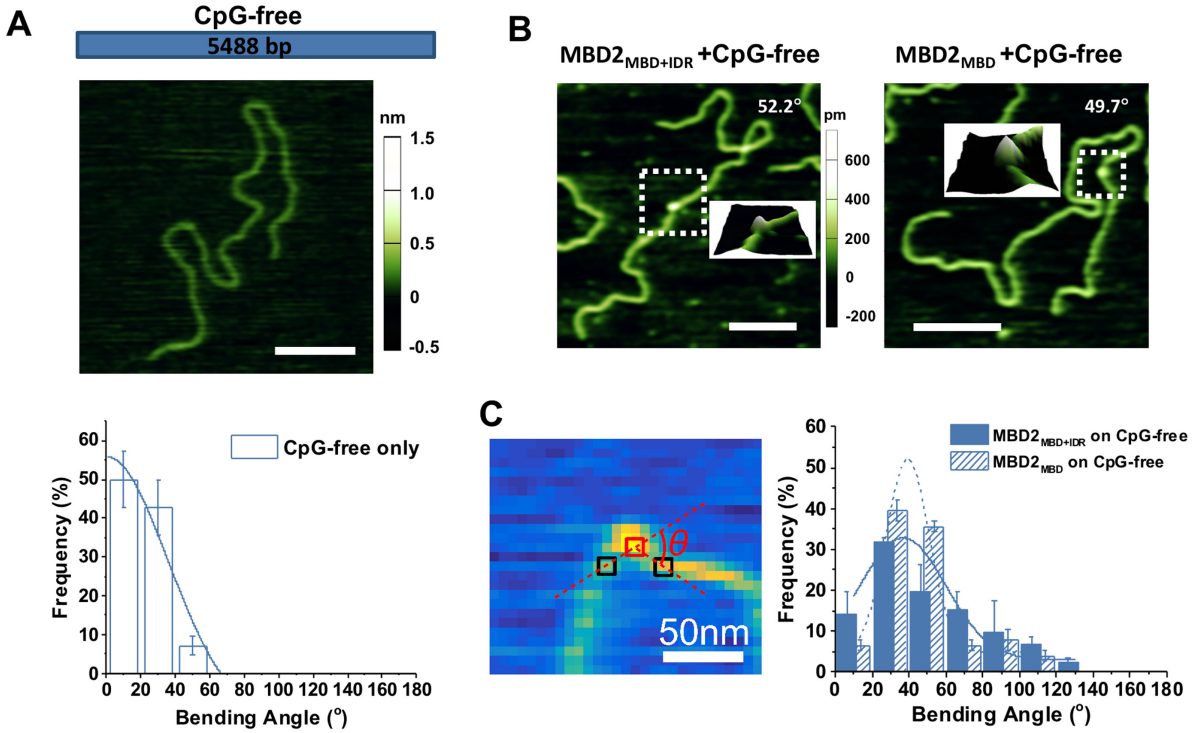

Figure 6. Bending angles induced by $MBD2_{MBD+IDR}$ and $MBD2_{MBD}$ on the linear CpG-free DNA substrate. (**A**) Cartoon drawing of the linear CpG-free DNA substrate (top panel), an AFM image of the linear CpG-free DNA (middle panel), and statistical analysis of the intrinsic DNA bending along the CpG-free DNA substrate (bottom panel). The solid line represent Gaussian fit to the data with the peak centered at 0°. (**B**) Representative AFM images of $MBD2_{MBD+IDR}$ (left panel) and $MBD2_{MBD}$ (right panel) on the CpG-free DNA substrate. Scale bars are at 200 nm. The inserts show the 3D surface plots of the zoomed (boxed) regions. (**C**) Statistical analysis of the DNA bending angles induced by $MBD2_{MBD+IDR}$ and $MBD2_{MBD}$ binding on the linear CpG-free DNA. The left panel shows an example of using the custom Matlab code to measure the DNA bending angle (red square: center of DNA-bound MBD2; black squares: DNA identified through sampling along a circle around the protein; θ: protein-mediated DNA bending angle. The solid and dotted lines in the right panel are Gaussian fits to the data ($R^2 > 0.90$) with peaks centered at 36.7° (±27.6°) for $MBD2_{MBD+IDR}$ ($N = 91$) and 39.2° (±13.7°) for $MBD2_{MBD}$ ($N = 77$) (Table 3).

Table 3. Summary of DNA bending angles induced by MBD2 binding

DNA		$MBD2_{MBD+IDR}$		$MBD2_{MBD}$	
		Bending angle (°)	*N*	Bending angle (°)	*N*
Unmethylated	CpG-free	36.7° ± 27.6°	91	39.2° ± 13.7°	77
	CpG-rich	66.4° ± 32.4°	167	68.8° ± 30.7°	102
	CpG free region	42.5° ± 26.3°	113	48.9° ± 20.1°	57
	CpG rich region	74.1° ± 35.7°	76	69.9° ± 36.1°	56
Methylated	CpG-free	N.A.		N.A.	
	CpG-rich	103.5° ± 23.1°	162	69.0° ± 32.6°	182
	CpG free region	42.1° ± 38.1°	105	41.4° ± 23.3°	181
	CpG rich region	102.2° ± 41.3°	73	62.6° ± 27.6°	114

The values represent mean ± SD from two to three experiments for each data set. The significance values regarding the difference among the data sets are reported in Supplementary Figure S8.

both $MBD2_{MBD+IDR}$ and $MBD2_{MBD}$ induced a similar degree of slight bending at the CpG-free region, upon binding to the methylated CpGs, $MBD2_{MBD+IDR}$ mediated additional DNA bending compared to $MBD2_{MBD}$ (Supplementary Figure S8D, Table 3). In summary, while the IDR region does not further modify the DNA bending by MBD2 at the CpG-free region or unmethylated CpG, it facilitates additional DNA bending upon recognition of the methylated CpG DNA (Supplementary Figure S9).

While $MBD2_{MBD}$ does not bend CpG-free DNA to the same extent as mCpG-rich DNA, it is unclear whether bending requires increased CpG content. Therefore, we isolated the CpG-poor region (0.6 CpG per 100 bp) and measured bending by $MBD2_{MBD+IDR}$ for both unmethylated and methylated DNA. Analysis of the bending angles (Supplementary Figure S10A,B) shows that $MBD2_{MBD+IDR}$ bends CpG-poor DNA (56.3° ± 24.7°), but somewhat less than CpG-rich DNA (66.4° ± 32.4°); and that methylation increases the bending (72.4° ± 60.7°), but not to the same extent as for CpG-rich DNA (103.5° ± 23.1°). This result indicates that the average of MBD2-mediated DNA bending depends on CpG density and methylation status.

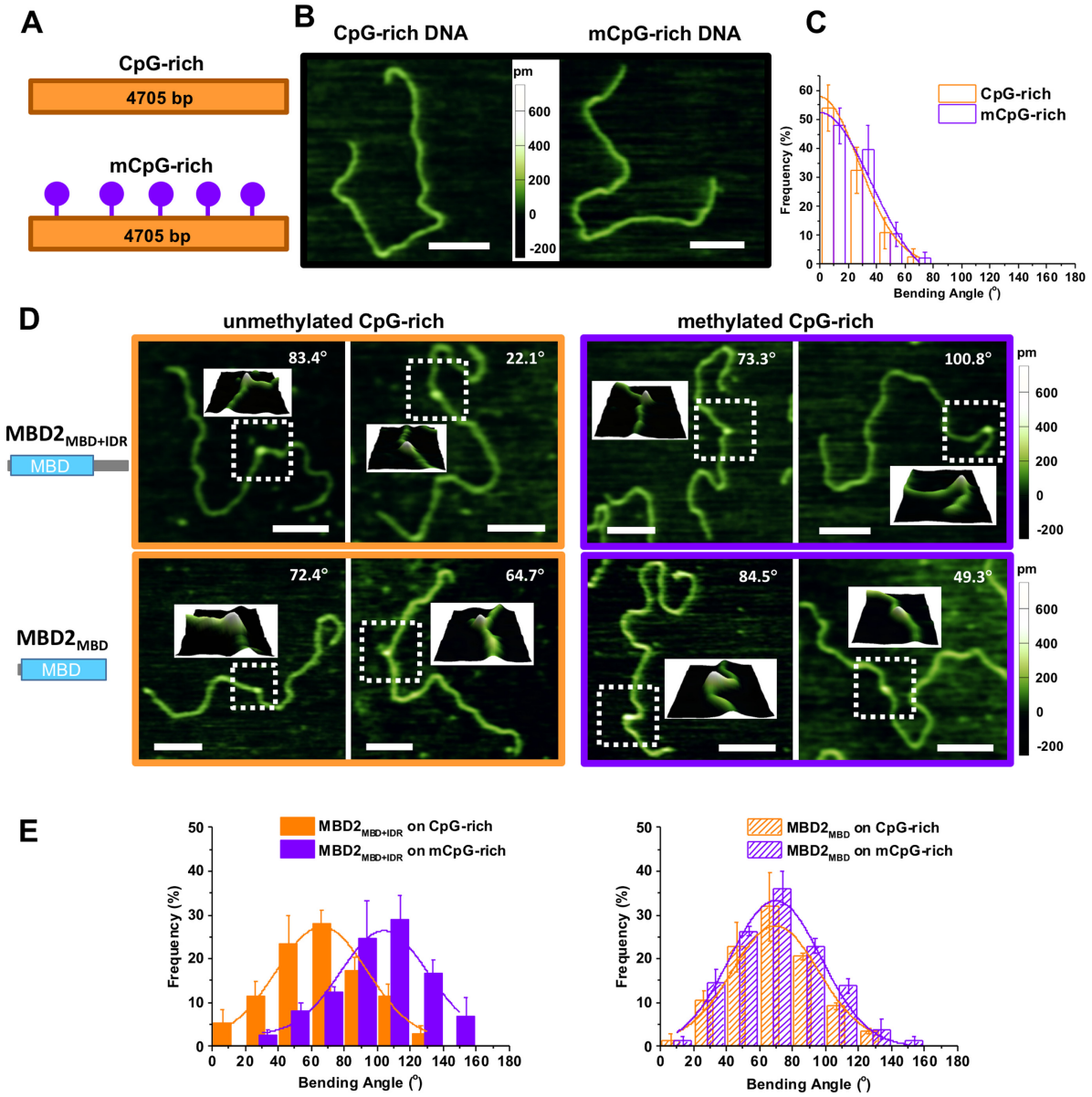

Figure 7. $MBD2_{MBD+IDR}$ but not $MBD2_{MBD}$ mediates additional DNA bending upon binding to mCpG-rich DNA. (**A**) Cartoon drawing of the linear unmethylated and methylated CpG-rich DNA substrates. (**B**) Representative AFM images of CpG-rich and mCpG-rich DNA only. (**C**) Statistical analysis of the intrinsic DNA bending along the CpG-rich and mCpG-rich DNA substrates. The solid lines represent Gaussian fits to the data with the peaks centered at 0°. (**D**) Representative AFM images of $MBD2_{MBD+IDR}$ (top panels) and $MBD2_{MBD}$ (bottom panels) binding to linear unmethylated (left panels) and methylated (right panels) CpG-rich DNA. Scale bars are at 200 nm. The inserts show the 3D surface plots of the zoomed (boxed) regions. (**E**) DNA bending angles upon binding of $MBD2_{MBD+IDR}$ (left panel) and $MBD2_{MBD}$ (right panel) to unmethylated (orange bars) and methylated (purple bars) CpG-rich DNA. The lines represent Gaussian fits to the data ($R^2 > 0.95$). The error bars represent SD. The mean and SEM of the bending angles are reported in Table 3.

Finally, given that we have high-resolution structural analysis, we chose to study the chicken MBD2 orthologue. While the human MBD2b and chicken MBD2 orthologues are highly homologous (94% identity for $MBD2_{MBD+IDR}$), we sought to confirm that the human $MBD2_{MBD+IDR}$ can bend methylated DNA as well. As expected, AFM of human $MBD2_{MBD+IDR}$ shows very similar bending to that of the chicken orthologue when bound to bound to CpG-free (51.5° ± 29.4°), CpG-rich (67.7° ± 27.2°) and mCpG-rich (96.8° ± 13.4°) DNA (Supplementary Figure S10C and D). Hence, the behavior we have characterized applies to the human orthologue as well.

DISCUSSION

The current model of MBD2 function postulates that the protein selectively targets methylated CpG islands, recruiting the NuRD co-regulatory complex to silence gene expression through histone deacetylase and nucleosome remodeling activities. However, genomic localization and gene expression studies have indicated that while MBD2-

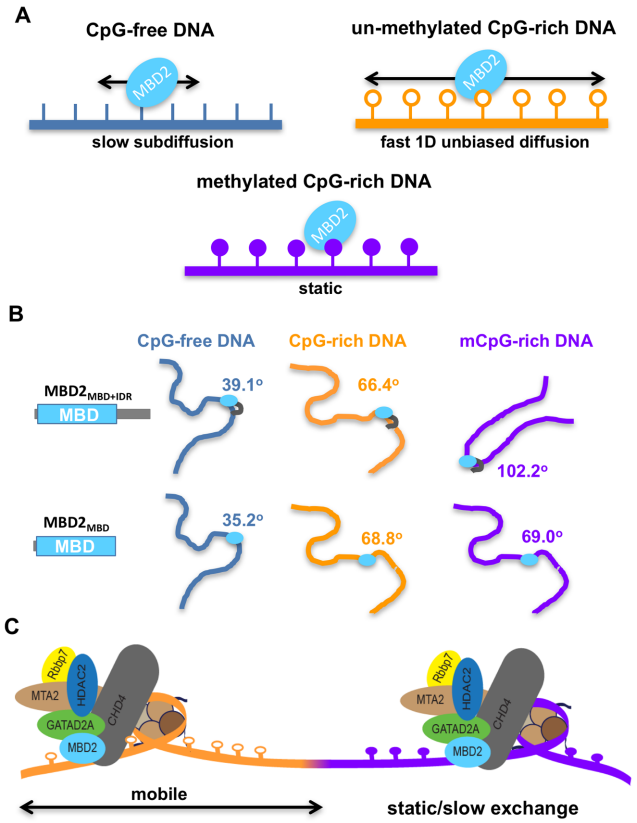

Figure 8. CpG and methylation-dependent DNA binding models of MBD2. (**A**) The difference in MBD2 DNA binding dynamics at CpG-free, CpG-rich and mCpG regions. MBD2 diffuses more rapidly and extensively on CpG-rich sequences than those that lack CpGs (CpG-free). MBD2 binds statically or with slower exchange rates when binding to mCpG-rich regions. (**B**) MBD2 recognizes CpG and mCpG through DNA bending. MBD2 induces sharper DNA bending at CpG-rich regions compared to at CpG-free, which is further augmented by IDR when binding to methylated CpG-rich sequences. The summary of the MBD2-induced DNA bending angles on different DNA substrates is presented in Table 3 and Supplementary Figure S9. (**C**) Proposed model for the dynamics of MBD2 in the context of the NuRD complex. MBD2 enables the NuRD complex to freely mobilize nucleosomes within unmethylated CpG islands, while impeding mobility on densely methylated CpG DNA.

NuRD predominately localizes to methylated CpG islands, it can be found at a subset of unmethylated CpG islands associated with active promoters (9,10,16,17). Interpretation of these results is further complicated by the low affinity MBD3 paralogue that likewise recruits NuRD complex in a mutually exclusive manner (30). These observations have led us to question whether MBD2-NuRD functions at both unmethylated and methylated promoters, contributing to either nucleosome mobilization or stabilization depending on the distinct dynamic DNA binding modes of the MBD2.

In the studies reported here, we have found that the isolated $MBD2_{MBD}$ shows at least three distinct DNA binding modes: (i) relatively slow 1D subdiffusion on CpG-free regions without significant DNA bending, (ii) relatively rapid 1D unbiased diffusion on unmethylated CpG-rich regions with intermediate DNA bending, (iii) stable binding on methylated CpG-rich regions associated with marked DNA bending (Figure 8A and B). Furthermore, results from tracking of MBD2 on DNA tightropes strongly support that MBD2 carries out curvilinear motion during rapid diffusion along the DNA, as has been described for other transcription factors (47–49). If the hydrodynamic radius of the red QD (655 nm) is assumed to be 11.5 nm (50) and the radius of gyration of free MBD2 is 1.28 nm based on the solution structure (13), then the expected upper limit for diffusion constants for a single red QD labeled MBD2 sliding on DNA is 21.1 $\mu m^2/s$. Assuming MBD2 rotates around DNA helix, the expected upper limits for diffusion constants based on the modified version of the Stokes-Einstein relation is 0.03 $\mu m^2/s$ (51), which is close to what was observed experimentally (Table 2). The associated IDR does not significantly change the 1D diffusion dynamics of MBD2, which is consistent with the notion that IDR does not change the structural recognition of mCpG or methylation selectivity supported by results from NMR experiments reported in the current and previous studies (11).

Once MBD2 enters densely methylated regions, however, diffusion is greatly restricted, manifested as stable DNA binding in fluorescence imaging (spatial resolution 16 nm) and slower exchange rates on methylated CpGs. The stable binding of both $MBD2_{MBD}$ and $MBD2_{MBD+IDR}$ on DNA tightropes containing methylated CpGs are consistent with previous observations. Binding analyses (6,13,52,53) and quantum mechanics calculations (54) have established that methylation contributes to a favorable change in free energy for MBD2 binding to DNA. In addition, computational studies suggest that methylation leads to subtle structural rearrangements within the DNA and MBD binding sites (54). These structural rearrangements and the free energy difference are consistent with the chemical shift changes we observe between methylation specific and non-specific binding modes and likely contribute to the marked stabilization of MBD2 when bound to methylated CpG regions as observed by single-molecule fluorescence. However, unexpectedly, this study uncovered a new role for the IDR in recognition of methylated DNA. Combining results from NMR and AFM experiments strongly supports that the IDR serves as an additional anchor by reducing exchange between CpG sites and dissociation from DNA leading to stable binding over a methylated CpG region, as well as introducing additional bending at methylated CpG sites.

Therefore, these data support a model of $MBD2_{MBD}$ function in which the dynamic mobility of this domain regulates whether MBD2-NuRD efficiently rearranges nucleosomes along an unmethylated CpG island or fixes nucleosomes in place within methylated CpG islands (Figure 8C). This difference suggests that MBD2-NuRD will tend to move nucleosomes away from unmethylated and towards methylated regions and allow for more dynamic mobility within unmethylated regions. Furthermore, AFM analyses clearly shows that MBD2 bends methylated DNA, an observation that has not been previously reported. Whether this bending occurs in the context of the full MBD2-NuRD complex and nucleosome laden chromatin is yet to be determined. Nonetheless, this observation raises the possibility that MBD2 itself contributes to DNA compaction.

Taken together, these results potentially shed light on the enigmatic function of MBD2-NuRD in cells. The established model that MBD2 solely targets NuRD to methy-

lated CpG islands and silences the associated genes based on previous biochemical and biophysical characterizations does not fit with recent whole genome localization studies and gene expression analyses (9,16,55). Instead, the cellular function of MBD2 appears to be context dependent, such that MBD2-NuRD can be associated with either gene activation or silencing, although predominantly the latter. If, however, one considers that the function of MBD2 reflects dynamic mobility on DNA as opposed to an on-off binding event, then the function is perhaps less enigmatic. Given both the relatively high affinity for non-methylated DNA as well as the presence of additional chromatin and DNA interacting domains within NuRD, then it is unlikely that the complex spends time dissociated from DNA. Instead, the complex most likely dynamically spreads across chromatin depending on the relative binding affinity and mobility of its constituent parts. Hence, MBD2 should allow the NuRD complex to freely mobilize nucleosomes within unmethylated CpG islands, while impeding mobility on densely methylated DNA. This model implies that MBD2-NuRD would accumulate both at densely methylated CpG islands as well as at the junction between unmethylated and methylated CpG rich regions. We suggest that the latter has been observed in ChIP analyses which revealed a peak for MBD2 localization at the shoulder of an unmethylated CpG island (i.e. Figure 5 B in Manefera *et al.* (16)). In fact, MBD2-NuRD accumulation at the edges of CpG islands helps explain the strong correlation between gene expression and differential methylation of CpG shores, the regions immediately adjacent to islands (56,57).

In summary, we have found that the methylcytosine binding domain of MBD2 exhibits distinct dynamic DNA binding mode depending on CpG density and methylation status. These results underscore the importance of understanding how DNA binding domains dynamically associate with DNA and suggest a model for MBD2 function in cells. We propose that relative binding affinity is an inadequate description of DNA binding domain interaction with DNA, especially in the case of the MBD proteins. The different dynamic binding modes are more relevant to the function of MBD proteins in the context of large macromolecular machines. Hence, extending these analyses to the larger NuRD complex will help elucidate the function of this complex in epigenetic transcription regulation, cell differentiation, and development.

SUPPLEMENTARY DATA

Supplementary Data are available at NAR Online.

ACKNOWLEDGEMENTS

We would like to thank the Weninger group at NCSU for technical support, and Changjiang You and Jacob Piehler at *Universität Osnabrück* for providing the NTA compound.

FUNDING

National Institutes of Health [R01-GM107559 to H.W. and R.R., P30-ES025128 Pilot Project to H.W., R01-GM098264 to D.W.]; National Science Foundation [DBI1353897 to R.R.]; North Carolina State University [Research and Innovation Seed Funding to H.W.]. Funding for open access charge: NIH [R01-GM107559 and R01-GM098264].
Conflict of interest statement. None declared.

REFERENCES

1. Ambrosi,C., Manzo,M. and Baubec,T. (2017) Dynamics and context-dependent roles of DNA methylation. *J. Mol. Biol.*, **429**, 1459–1475.
2. Suzuki,M.M. and Bird,A. (2008) DNA methylation landscapes: provocative insights from epigenomics. *Nat. Rev. Genet.*, **9**, 465–476.
3. Kanwal,R. and Gupta,S. (2012) Epigenetic modifications in cancer. *Clin. Genet.*, **81**, 303–311.
4. Deaton,A.M. and Bird,A. (2011) CpG islands and the regulation of transcription. *Genes Dev.*, **25**, 1010–1022.
5. Illingworth,R.S. and Bird,A.P. (2009) CpG islands–'a rough guide'. *FEBS Lett.*, **583**, 1713–1720.
6. Hendrich,B. and Bird,A. (1998) Identification and characterization of a family of mammalian methyl-CpG binding proteins. *Mol. Cell. Biol.*, **18**, 6538–6547.
7. Hendrich,B. and Tweedie,S. (2003) The methyl-CpG binding domain and the evolving role of DNA methylation in animals. *Trends Genet.*, **19**, 269–277.
8. Zhang,Y., Ng,H.H., Erdjument-Bromage,H., Tempst,P., Bird,A. and Reinberg,D. (1999) Analysis of the NuRD subunits reveals a histone deacetylase core complex and a connection with DNA methylation. *Genes Dev.*, **13**, 1924–1935.
9. Baubec,T., Ivánek,R., Lienert,F. and Schübeler,D. (2013) Methylation-dependent and -independent genomic targeting principles of the MBD protein family. *Cell*, **153**, 480–492.
10. Günther,K., Rust,M., Leers,J., Boettger,T., Scharfe,M., Jarek,M., Bartkuhn,M. and Renkawitz,R. (2013) Differential roles for MBD2 and MBD3 at methylated CpG islands, active promoters and binding to exon sequences. *Nucleic Acids Res.*, **41**, 3010–3021.
11. Desai,M.A., Webb,H.D., Sinanan,L.M., Scarsdale,J.N., Walavalkar,N.M., Ginder,G.D. and Williams,D.C. Jr (2015) An intrinsically disordered region of methyl-CpG binding domain protein 2 (MBD2) recruits the histone deacetylase core of the NuRD complex. *Nucleic Acids Res.*, **43**, 3100–3113.
12. Bird,A.P. (1986) CpG-rich islands and the function of DNA methylation. *Nature*, **321**, 209–213.
13. Scarsdale,J.N., Webb,H.D., Ginder,G.D. and Williams,D.C. Jr (2011) Solution structure and dynamic analysis of chicken MBD2 methyl binding domain bound to a target-methylated DNA sequence. *Nucleic Acids Res.*, **39**, 6741–6752.
14. Cramer,J.M., Scarsdale,J.N., Walavalkar,N.M., Buchwald,W.A., Ginder,G.D. and Williams,D.C. Jr (2014) Probing the dynamic distribution of bound states for methylcytosine-binding domains on DNA. *J. Biol. Chem.*, **289**, 1294–1302.
15. Walavalkar,N.M., Cramer,J.M., Buchwald,W.A., Scarsdale,J.N. and Williams,D.C. Jr (2014) Solution structure and intramolecular exchange of methyl-cytosine binding domain protein 4 (MBD4) on DNA suggests a mechanism to scan for mCpG/TpG mismatches. *Nucleic Acids Res.*, **42**, 11218–11232.
16. Menafra,R., Brinkman,A.B., Matarese,F., Franci,G., Bartels,S.J.J., Nguyen,L., Shimbo,T., Wade,P.A., Hubner,N.C. and Stunnenberg,H.G. (2014) Genome-wide binding of MBD2 reveals strong preference for highly methylated loci. *PLoS ONE*, **9**, e99603.
17. Shimbo,T., Du,Y., Grimm,S.A., Dhasarathy,A., Mav,D., Shah,R.R., Shi,H. and Wade,P.A. (2013) MBD3 localizes at promoters, gene bodies and enhancers of active genes. *PLoS Genet.*, **9**, e1004028.
18. Gorman,J., Plys,A.J., Visnapuu,M.-L., Alani,E. and Greene,E.C. (2010) Visualizing one-dimensional diffusion of eukaryotic DNA repair factors along a chromatin lattice. *Nat. Struct. Mol. Biol.*, **17**, 932–938.
19. Gorman,J. and Greene,E.C. (2008) Visualizing one-dimensional diffusion of proteins along DNA. *Nat. Struct. Mol. Biol.*, **15**, 768–774.
20. Zweckstetter,M. and Bax,A. (2001) Characterization of molecular alignment in aqueous suspensions of Pf1 bacteriophage. *J. Biomol. NMR*, **20**, 365–377.
21. Clore,G.M., Starich,M.R. and Gronenborn,A.M. (1998) Measurement of residual dipolar couplings of macromolecules

aligned in the nematic phase of a colloidal suspension of rod-shaped viruses. *J. Am. Chem. Soc.*, **120**, 10571–10572.
22. Delaglio,F., Grzesiek,S., Vuister,G.W., Zhu,G., Pfeifer,J. and Bax,A. (1995) NMRPipe: a multidimensional spectral processing system based on UNIX pipes. *J. Biomol. NMR*, **6**, 277–293.
23. Skinner,S.P., Goult,B.T., Fogh,R.H., Boucher,W., Stevens,T.J., Laue,E.D. and Vuister,G.W. (2015) Structure calculation, refinement and validation using *CcpNmr Analysis*. *Acta Crystallogr. D Biol. Crystallogr.*, **71**, 154–161.
24. Vranken,W.F., Boucher,W., Stevens,T.J., Fogh,R.H., Pajon,A., Llinas,M., Ulrich,E.L., Markley,J.L., Ionides,J. and Laue,E.D. (2005) The CCPN data model for NMR spectroscopy: development of a software pipeline. *Proteins*, **59**, 687–696.
25. Sahu,D., Clore,G.M. and Iwahara,J. (2007) TROSY-based z-exchange spectroscopy: application to the determination of the activation energy for intermolecular protein translocation between specific sites on different DNA molecules. *J. Am. Chem. Soc.*, **129**, 13232–13237.
26. Lopez-Serra,L., Ballestar,E., Fraga,M.F., Alaminos,M., Setien,F. and Esteller,M. (2006) A profile of methyl-CpG binding domain protein occupancy of hypermethylated promoter CpG islands of tumor suppressor genes in human cancer. *Cancer Res.*, **66**, 8342–8346.
27. Reichel,A., Schaible,D., Furoukh,Al N., Cohen,M., Schreiber,G. and Piehler,J. (2007) Noncovalent, site-specific biotinylation of histidine-tagged proteins. *Anal. Chem.*, **79**, 8590–8600.
28. Lin,J., Countryman,P., Buncher,N., Kaur,P., E,L., Zhang,Y., Gibson,G., You,C., Watkins,S.C., Piehler,J. *et al.* (2014) TRF1 and TRF2 use different mechanisms to find telomeric DNA but share a novel mechanism to search for protein partners at telomeres. *Nucleic Acids Res.*, **42**, 2493–2504.
29. Saxton,M.J. (1997) Single-particle tracking: the distribution of diffusion coefficients. *Biophys. J.*, **72**, 1744–1753.
30. Le Guezennec,X., Vermeulen,M., Brinkman,A.B., Hoeijmakers,W.A.M., Cohen,A., Lasonder,E. and Stunnenberg,H.G. (2006) MBD2/NuRD and MBD3/NuRD, two distinct complexes with different biochemical and functional properties. *Mol. Cell. Biol.*, **26**, 843–851.
31. Cramer,J.M., Pohlmann,D., Gomez,F., Mark,L., Kornegay,B., Hall,C., Siraliev-Perez,E., Walavalkar,N.M., Sperlazza,M.J., Bilinovich,S. *et al.* (2017) Methylation specific targeting of a chromatin remodeling complex from sponges to humans. *Sci. Rep.*, **7**, 1–15.
32. Winter,R.B. and von Hippel,P.H. (1981) Diffusion-driven mechanisms of protein translocation on nucleic acids. 2. The Escherichia coli repressor–operator interaction: equilibrium measurements. *Biochemistry*, **20**, 6948–6960.
33. Berg,O.G., Winter,R.B. and von Hippel,P.H. (1981) Diffusion-driven mechanisms of protein translocation on nucleic acids. 1. Models and theory. *Biochemistry*, **20**, 6929–6948.
34. Winter,R.B., Berg,O.G. and von Hippel,P.H. (1981) Diffusion-driven mechanisms of protein translocation on nucleic acids. 3. The Escherichia coli lac repressor–operator interaction: kinetic measurements and conclusions. *Biochemistry*, **20**, 6961–6977.
35. von Hippel,P.H. and Berg,O.G. (1989) Facilitated target location in biological systems. *J. Biol. Chem.*, **264**, 675–678.
36. Tafvizi,A., Mirny,L.A. and van Oijen,A.M. (2011) Dancing on DNA: kinetic aspects of search processes on DNA. *ChemPhysChem*, **12**, 1481–1489.
37. Allen,H.F., Wade,P.A. and Kutateladze,T.G. (2013) The NuRD architecture. *Cell. Mol. Life Sci.*, **70**, 3513–3524.
38. Lai,A.Y. and Wade,P.A. (2011) Cancer biology and NuRD: a multifaceted chromatin remodelling complex. *Nat. Rev. Cancer*, **11**, 588–596.
39. Dunn,A.R., Kad,N.M., Nelson,S.R., Warshaw,D.M. and Wallace,S.S. (2011) Single Qdot-labeled glycosylase molecules use a wedge amino acid to probe for lesions while scanning along DNA. *Nucleic Acids Res.*, **39**, 7487–7498.
40. Hughes,C.D., Wang,H., Ghodke,H., Simons,M., Towheed,A., Peng,Y., Van Houten,B. and Kad,N.M. (2013) Real-time single-molecule imaging reveals a direct interaction between UvrC and UvrB on DNA tightropes. *Nucleic Acids Res.*, **41**, 4901–4912.
41. Kad,N.M., Wang,H., Kennedy,G.G., Warshaw,D.M. and Van Houten,B. (2010) Collaborative dynamic DNA scanning by nucleotide excision repair proteins investigated by single-molecule imaging of quantum-dot-labeled proteins. *Mol. Cell*, **37**, 702–713.
42. Lata,S. and Piehler,J. (2005) Stable and functional immobilization of histidine-tagged proteins via multivalent chelator headgroups on a molecular poly(ethylene glycol) brush. *Anal. Chem.*, **77**, 1096–1105.
43. Kaur,P., Plochberger,B., Costa,P., Cope,S.M., Vaiana,S.M. and Lindsay,S. (2012) Hydrophobicity of methylated DNA as a possible mechanism for gene silencing. *Phys. Biol.*, **9**, 065001.
44. Rule,G.S. and Hitchens,T.K. (2006) *Fundamentals of protein NMR spectroscopy*. Springer, Vol. **5**, pp. 1–531.
45. Iwahara,J. and Clore,G.M. (2006) Direct observation of enhanced translocation of a homeodomain between DNA cognate sites by NMR exchange spectroscopy. *J. Am. Chem. Soc.*, **128**, 404–405.
46. Iwahara,J., Zweckstetter,M. and Clore,G.M. (2006) NMR structural and kinetic characterization of a homeodomain diffusing and hopping on nonspecific DNA. *Proc. Natl. Acad. Sci. U.S.A.*, **103**, 15062–15067.
47. Blainey,P.C., Luo,G., Kou,S.C., Mangel,W.F., Verdine,G.L., Bagchi,B. and Xie,X.S. (2009) Nonspecifically bound proteins spin while diffusing along DNA. *Nat. Struct. Mol. Biol.*, **16**, 1224–1229.
48. Dikić,J., Menges,C., Clarke,S., Kokkinidis,M., Pingoud,A., Wende,W. and Desbiolles,P. (2012) The rotation-coupled sliding of EcoRV. *Nucleic Acids Res.*, **40**, 4064–4070.
49. Marklund,E.G., Mahmutovic,A., Berg,O.G., Hammar,P., van der Spoel,D., Fange,D. and Elf,J. (2013) Transcription-factor binding and sliding on DNA studied using micro- and macroscopic models. *Proc. Natl. Acad. Sci. U.S.A.*, **110**, 19796–19801.
50. Arnspang,E.C., Brewer,J.R. and Lagerholm,B.C. (2012) Multi-color single particle tracking with quantum dots. *PLoS ONE*, **7**, e48521.
51. Schurr,J.M. (1975) The one-dimensional diffusion coefficient of proteins absorbed on DNA hydrodynamic considerations. *Biophys. Chem.*, **9**, 413–414.
52. Hashimoto,H., Liu,Y., Upadhyay,A.K., Chang,Y., Howerton,S.B., Vertino,P.M., Zhang,X. and Cheng,X. (2012) Recognition and potential mechanisms for replication and erasure of cytosine hydroxymethylation. *Nucleic Acids Res.*, **40**, 4841–4849.
53. Fraga,M.F., Ballestar,E., Montoya,G., Taysavang,P., Wade,P.A. and Esteller,M. (2003) The affinity of different MBD proteins for a specific methylated locus depends on their intrinsic binding properties. *Nucleic Acids Res.*, **31**, 1765–1774.
54. Zou,X., Ma,W., Solov'yov,I.A., Chipot,C. and Schulten,K. (2012) Recognition of methylated DNA through methyl-CpG binding domain proteins. *Nucleic Acids Res.*, **40**, 2747–2758.
55. Menafra,R. and Stunnenberg,H.G. (2014) MBD2 and MBD3: elusive functions and mechanisms. *Front Genet.*, **5**, 428.
56. Irizarry,R.A., Ladd-Acosta,C., Wen,B., Wu,Z., Montano,C., Onyango,P., Cui,H., Gabo,K., Rongione,M., Webster,M. *et al.* (2009) The human colon cancer methylome shows similar hypo- and hypermethylation at conserved tissue-specific CpG island shores. *Nat. Genet.*, **41**, 178–186.
57. Doi,A., Park,I.-H., Wen,B., Murakami,P., Aryee,M.J., Irizarry,R., Herb,B., Ladd-Acosta,C., Rho,J., Loewer,S. *et al.* (2009) Differential methylation of tissue- and cancer-specific CpG island shores distinguishes human induced pluripotent stem cells, embryonic stem cells and fibroblasts. *Nat. Genet.*, **41**, 1350–1353.

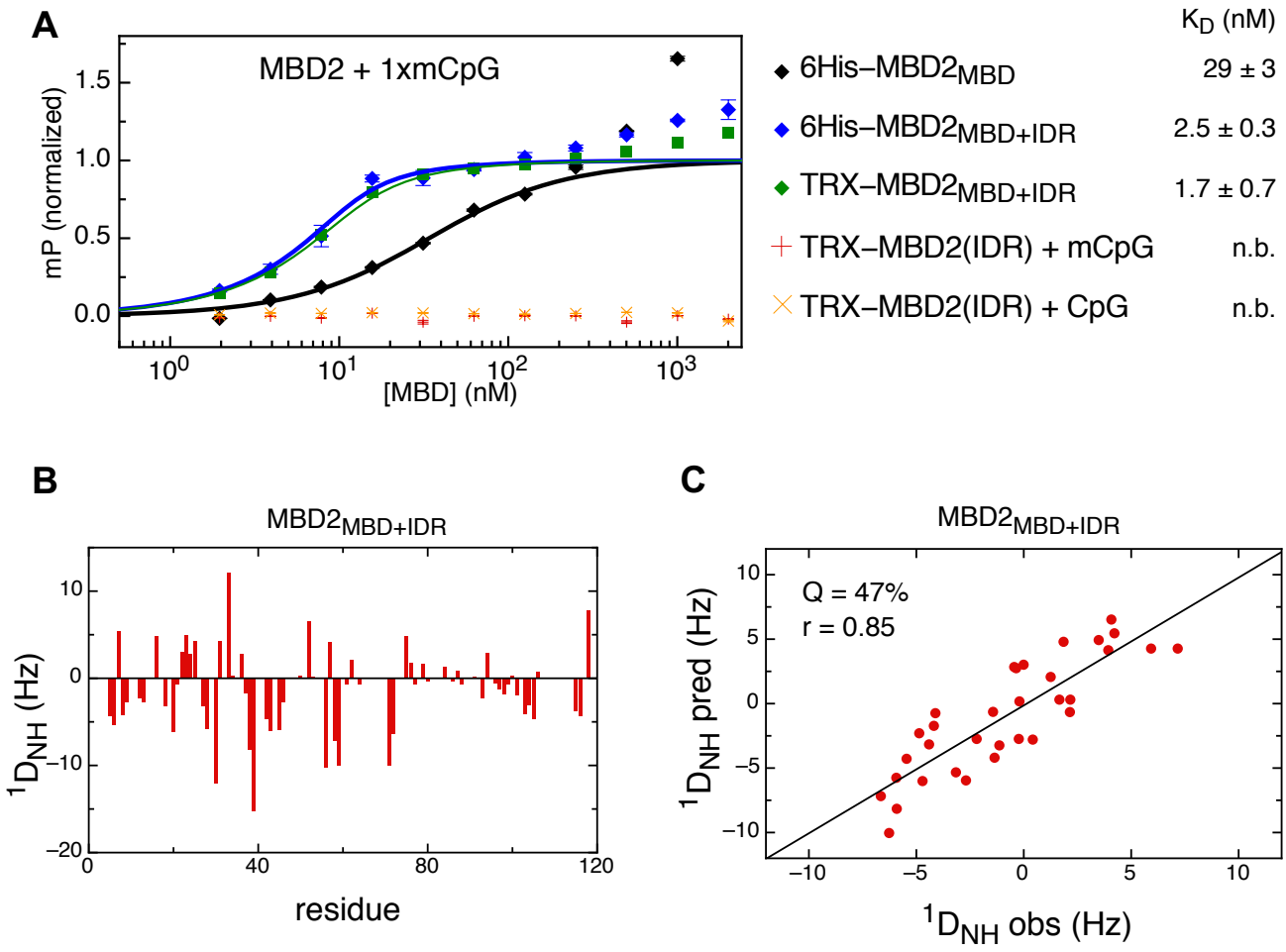

Supplementary Figure S1. Binding affinity and NMR analyses of $MBD2_{MBD}$ and $MBD2_{MBD+IDR}$ (**A**) The binding affinity for methylated DNA was determined by fluorescence polarization analysis for $MDB2_{MBD}$ and $MBD2_{MBD+IDR}$ with and without a thioredoxin (TRX) tag. Each titration shows evidence of non-specific binding to DNA at higher protein concentrations, typical of MBDs. We excluded these latter data points from the fit and normalized the data to 1.0. In addition, binding to methylated (mCpG) and unmethyated (CpG) DNA was measured for the full intrinsically disordered region, TRX-MBD2(IDR), that lacks the MBD. As expected, the IDR does not bind DNA in isolation. (**B**) ^{15}NH residual dipolar couplings ($^1D_{NH}$) were measured for $MBD2_{MBD+IDR}$ bound to methylated DNA and (**C**) fit to the known structure of the $MBD2_{MBD}$.

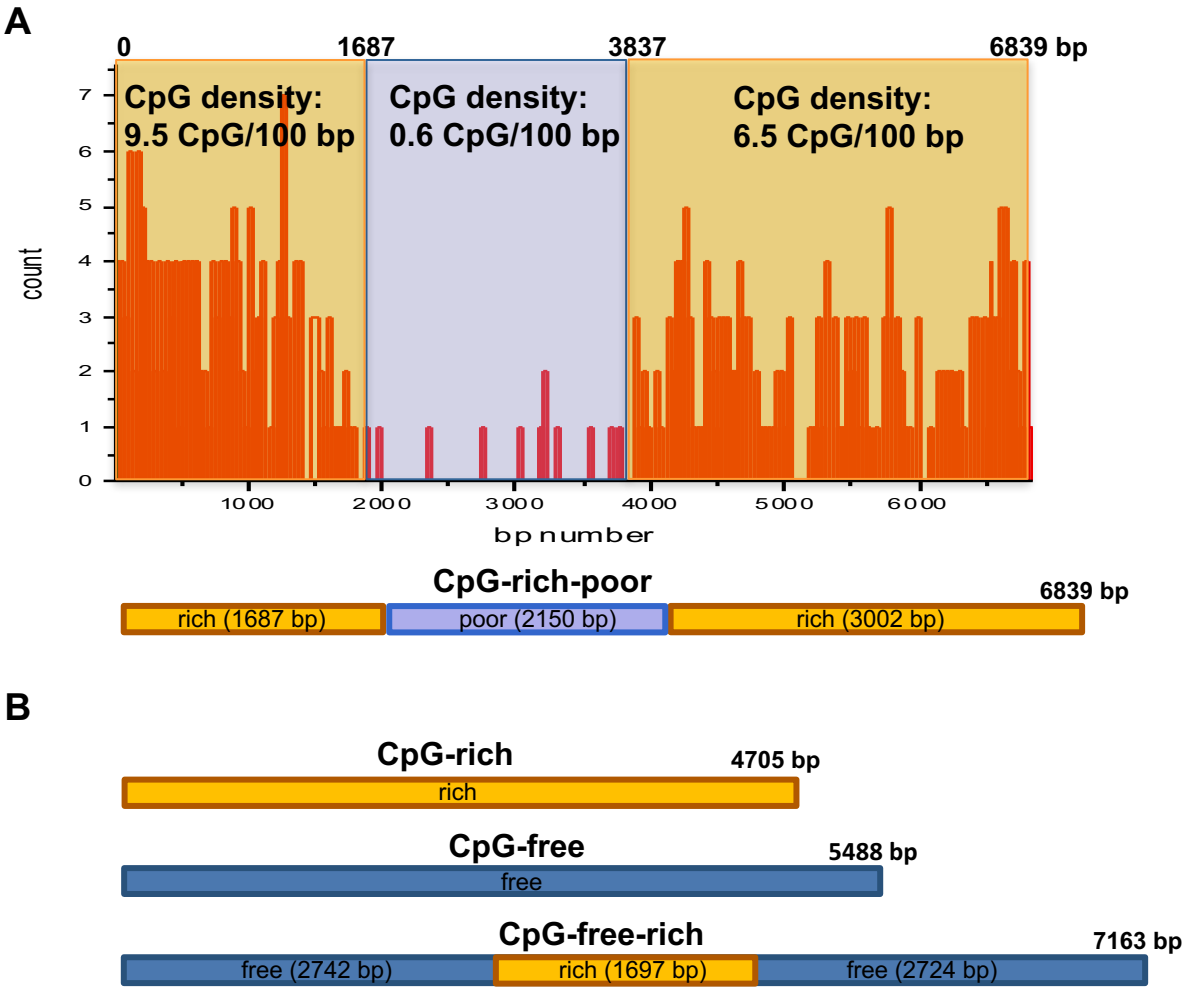

Supplementary Figure S2. Summary of the DNA substrates used for the DNA tightrope assay and AFM imaging. (**A**) The map and density of the CpG site on the CpG-rich-poor DNA substrate. (**B**) Diagrams of DNA substrates used for AFM imaging and in ligation reactions for the DNA tightrope assay. The linear CpG-rich DNA (4705 bp) was generated by restriction digestion with NcoI. The linear CpG-free and CpG-free-rich were obtained by restriction digestion of the plasmid DNA with StuI. DNA was purified using the Qiagen PCR kit.

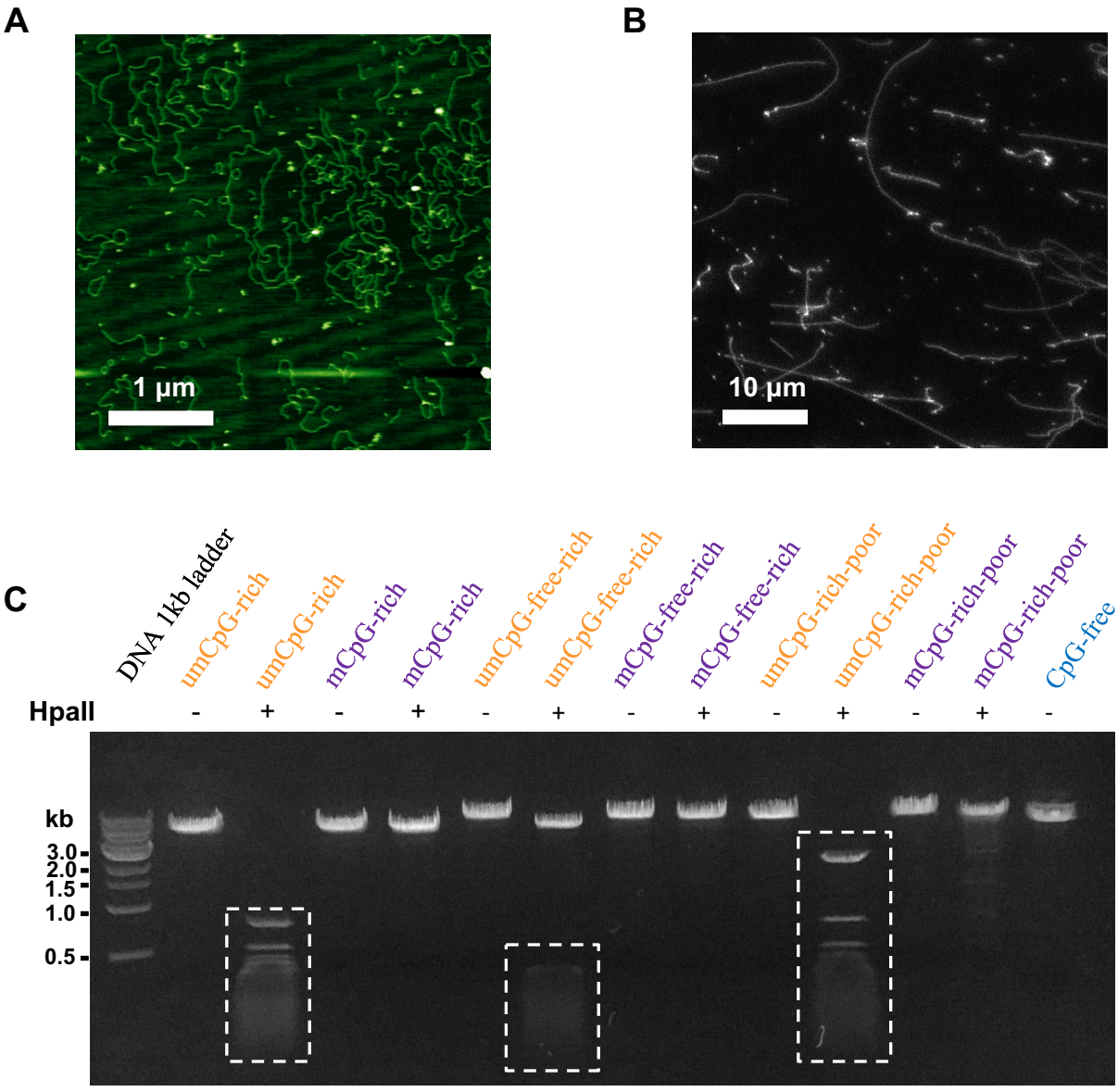

Supplementary Figure S3. Quantification of ligation and methylation efficiency. A representative (**A**) AFM image of ligated mCpG-rich DNA on a mica surface and **(B)** fluorescence image of YOYO1-stained ligated mCpG-rich DNA substrate on an APTES-treated cover slide. (**C**) Confirmation of DNA methylation through HpaII restriction digestion. The boxed regions indicate digested DNA fragments from unmethylated DNA.

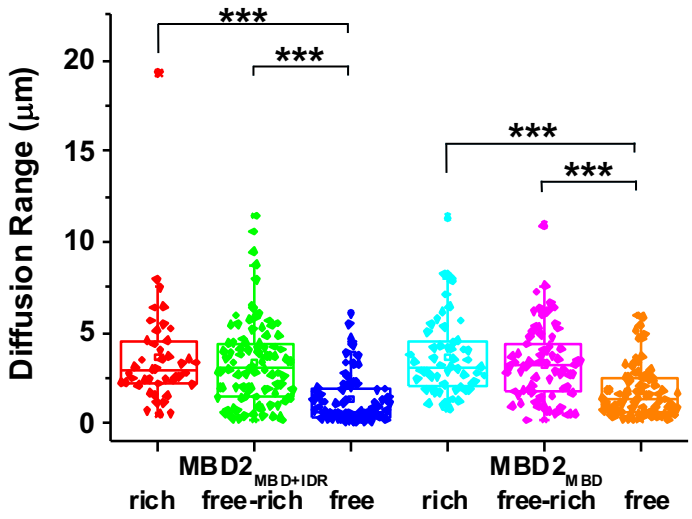

Supplementary Figure S4. Diffusion ranges of $MBD2_{MBD+IDR}$ and $MBD2_{MBD}$ on three DNA substrates. The diffusion range of $MBD2_{MBD+IDR}$ is 3.64 (±0.45) μm on CpG-rich, 3.32 (±0.23) μm on CpG-free-rich, and 1.31 (±0.13) μm on CpG-free. For $MBD2_{MBD}$, the diffusion range is 3.67 (±0.29) μm on CpG-rich, 3.27 (±0.24) μm on CpG-free-rich, and 1.77 (±0.15) μm on CpG-free. *: $p < 0.05$; **: $p < 0.005$; ***$p < 0.0005$.

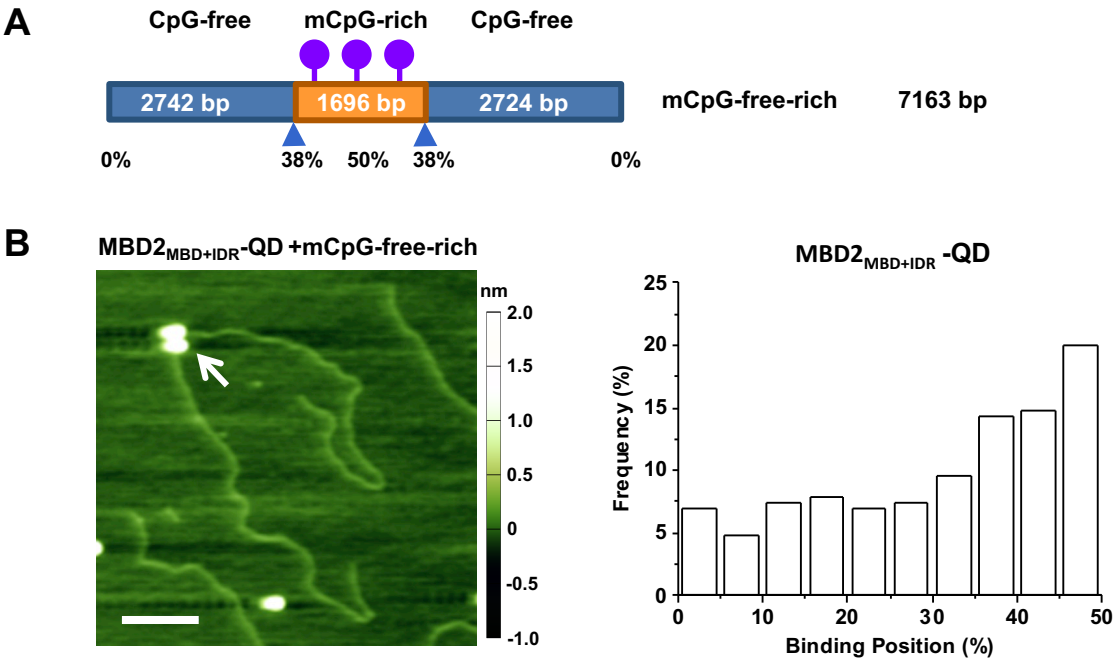

Supplementary Figure S5. QD-labeled $MBD2_{MBD+IDR}$ retains binding specificity for methylated CpG sites. (**A**) Cartoon drawing of the DNA substrate. (**B**) AFM imaging of $MDB2_{MBD+IDR}$-QD on linear mCpG-free-rich DNA substrate. Left panel: an AFM topographic image with a white arrow pointing to a $MBD2_{MBD+IDR}$-QD complex on DNA. The scale bar represents 200 nm. Right panel: the binding position of $MBD2_{MBD+IRD}$-QD complex on the linear mCpG-free-rich DNA substrate. Binding position analysis shows that over 49% of $MBD2_{MBD+IDR}$-QD (N=113 out of 230) binds to the methylated CpG-rich region (38% to 50% on mCpG-free-rich DNA).

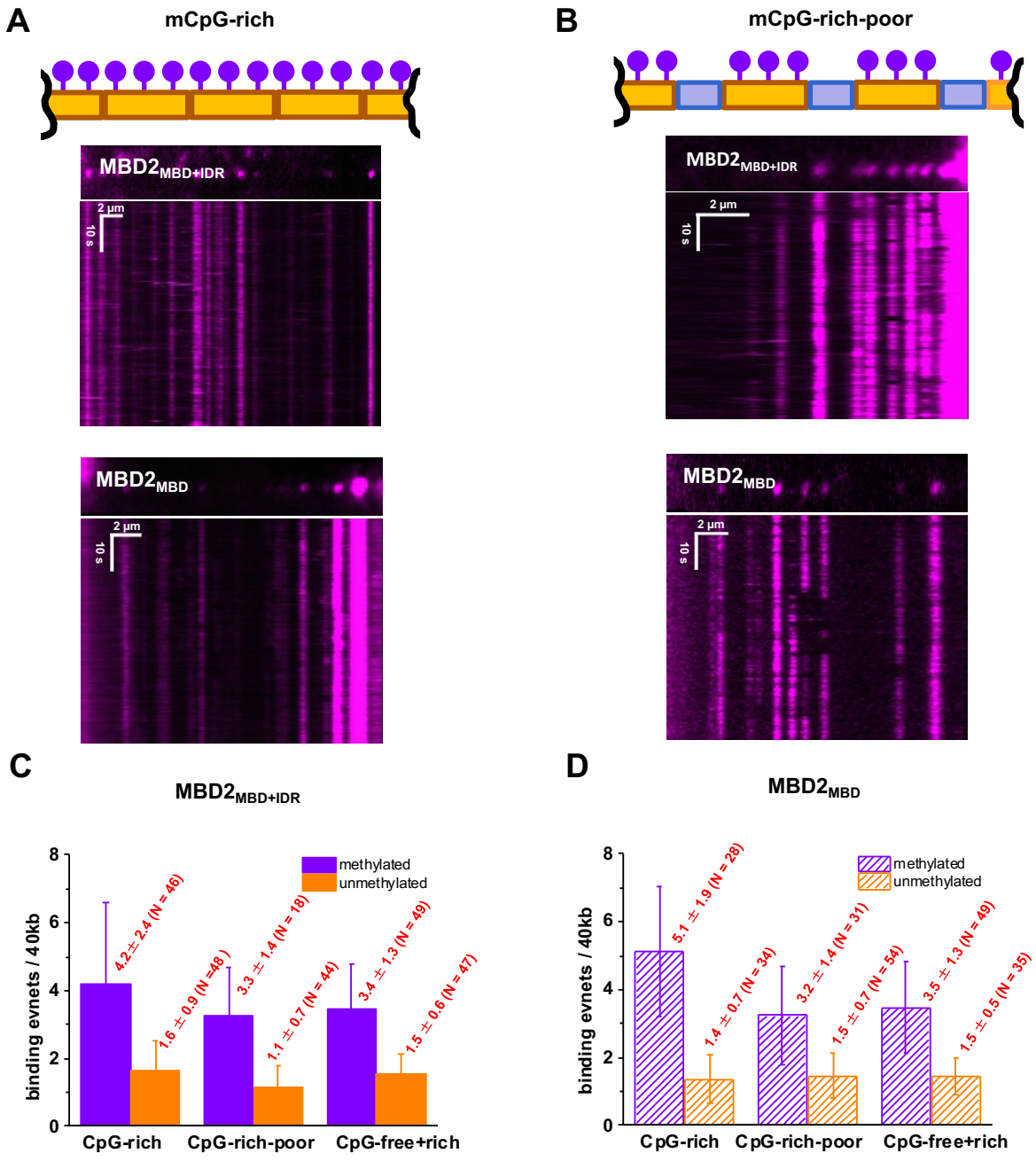

Supplementary Figure S6. Both $MBD2_{MBD+IDR}$ and $MBD2_{MBD}$ become static on methylated CpG-rich and CpG-rich-poor DNA substrates. (**A** and **B**) Top panels: cartoon drawing of the ligated DNA substrates using in the DNA tightrope assay. Middle and bottom panels: examples of individual DNA tightropes with QD-labeled proteins showing fluorescence images at the top and kymographs at the bottom. (**C** and **D**) The number of MBD2 complexes observed on DNA tightropes per 40 kb. The numbers in **C** ($MBD2_{MBD+IDR}$) and **D** ($MBD2_{MBD}$) report the mean±S.D. and the number of DNA tightropes analyzed. The average and SEM of the unmethylated and methylated DNA tightrope lengths are 12.3±0.4 μm (~38. 4 kb) and 11.1±0.3 μm (~34.7 kb), respectively.

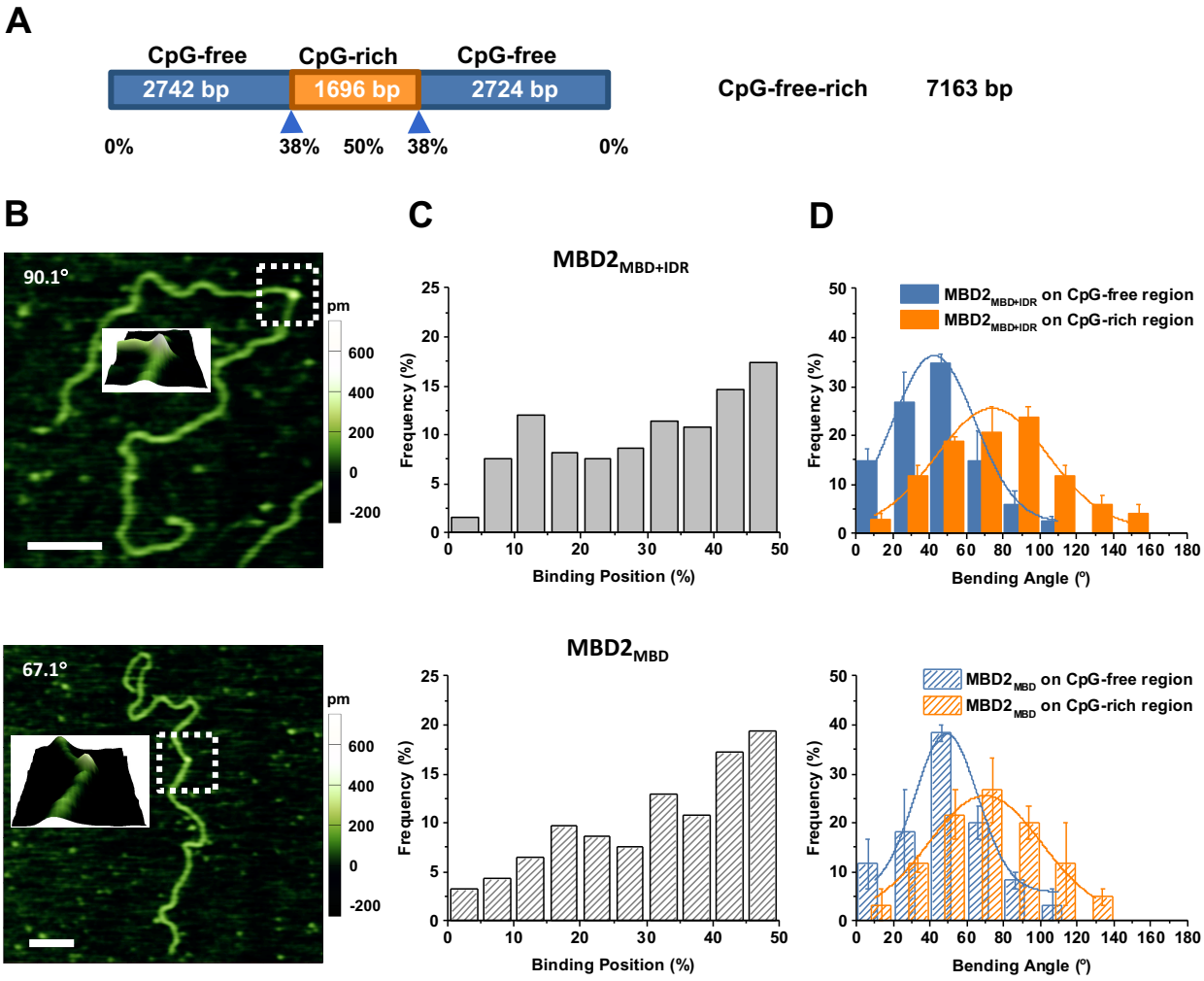

Supplementary Figure S7. Both $MBD2_{MBD+IDR}$ and $MBD2_{MBD}$ induce additional bending at the unmethylated CpG-rich region compared to binding at CpG-free regions. (**A**) Cartoon drawing of the CpG-free-rich DNA substrate. (**B**) AFM images of $MDB2_{MBD+IDR}$ (top panel) and $MBD2_{MBD}$ (bottom panel) on linear CpG-free rich substrate. The inserts show the 3D surface plots of the expanded (boxed) regions. The numbers in the images show the DNA bending angles at MBD binding sites. (**C**) Analysis of the binding position of $MDB2_{MBD+IDR}$ (top panel) and $MBD2_{MBD}$ (bottom panel) on linear CpG-free-rich substrate. Binding position analysis shows that over 42% of $MBD2_{MBD+IDR}$ (N = 79 out of 184) and 47% of $MBD2_{MBD}$ (N=44 out of 93) binds to the CpG-rich region (38% to 50%). (**D**) Analysis of the DNA bending angle induced by $MBD2_{MBD+IDR}$ and $MBD2_{MBD}$ at the CpG-free (0% to 38%) and CpG-rich regions (38% to 50%). The solid lines are Gaussian fits to the data (R^2> 0.97). The bending angles induced upon MBD protein binding are 42.5°±26.3° (N=113) and 74.1°±35.7° (N=76) for $MBD2_{MBD+IDR}$, 48.9°±20.1° (N=57) and 69.9°±36.1°(N=56) for $MBD2_{MBD}$ at CpG-free and CpG-rich regions, respectively.

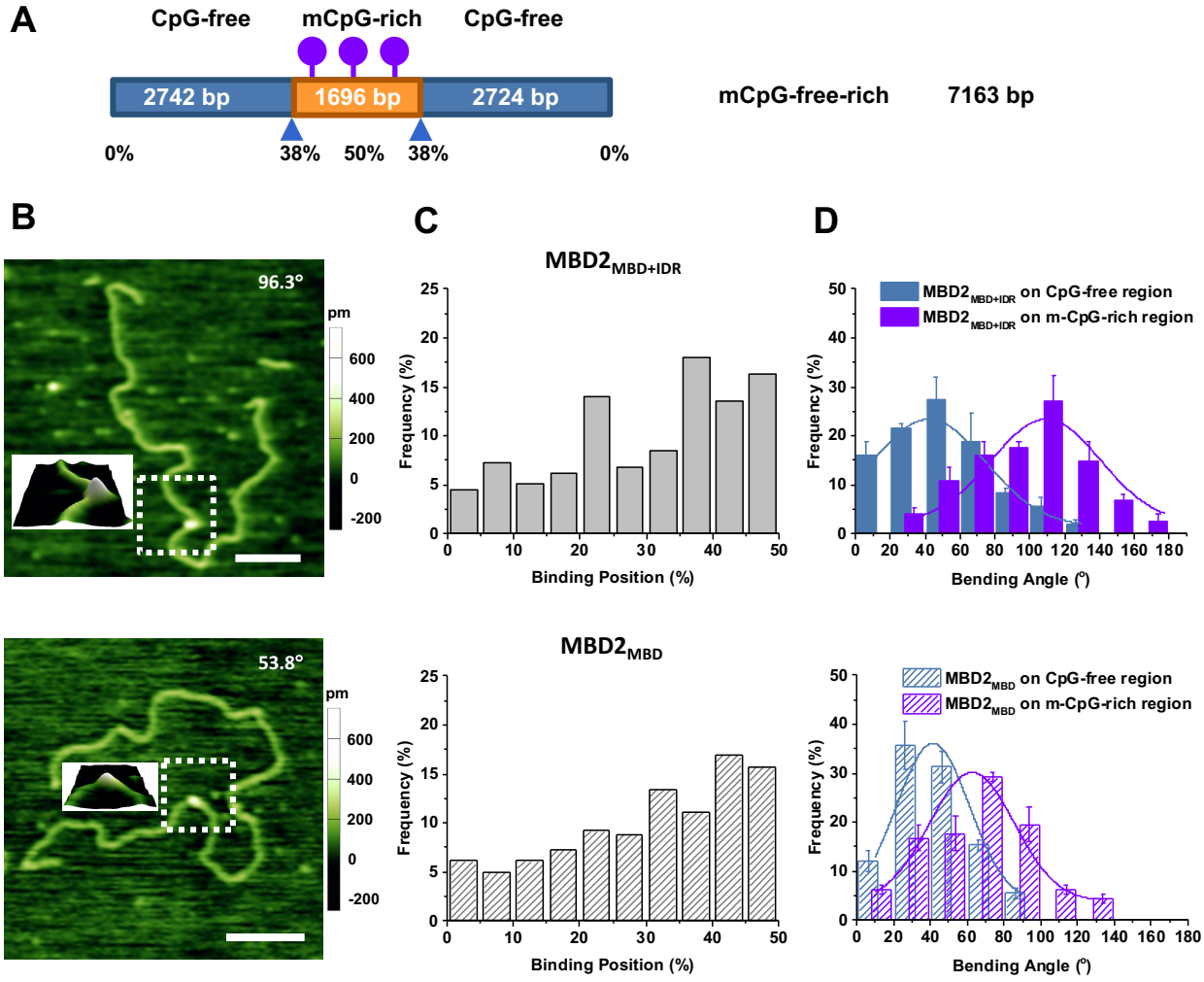

Supplementary Figure S8. Direct comparison of DNA bending upon binding of $MBD2_{MBD+IDR}$ and $MBD2_{MBD}$ to CpG-free and mCpG-rich regions in the mCpG-free-rich DNA substrate. (**A**) Cartoon drawing of the mCpG-free-rich DNA substrate. (**B**) AFM images of $MDB2_{MBD+IDR}$ (top panel) and $MBD2_{MBD}$ (bottom panel) on linear mCpG-free rich substrate. The inserts show the 3D surface plots of the expanded (boxed) regions. The numbers in the images show the DNA bending angles at MBD binding sites. (**C**) Analysis of the binding position of $MDB2_{MBD+IDR}$ (top panel) and $MBD2_{MBD}$ (bottom panel) on the linear mCpG-free-rich substrate. Binding position analysis shows that over 47% of $MBD2_{MBD+IDR}$ (N = 85 out of 178) and 43% of $MBD2_{MBD}$ (N=114 out of 260) binds to the methylated mCpG rich region (38% to 50%). (**D**) Analysis of the DNA bending angle induced by $MBD2_{MBD+IDR}$ and $MBD2_{MBD}$ at the CpG-free (0% to 38%) and mCpG-rich regions (38% to 50%). The solid lines in the right panels are Gaussian fits to the data (R^2 >0.90) with the peaks centered at 42.1°(±38.1°, N=105) at the CpG-free region and 102.2° (±41.3°, N=73) at the mCpG-rich region for $MBD2_{MBD+IDR}$, and 41.4° (±23.3°, N=181) at the CpG-free region and 62.6° (±27.6°, N=114) at the CpG-rich region for $MBD2_{MBD}$.

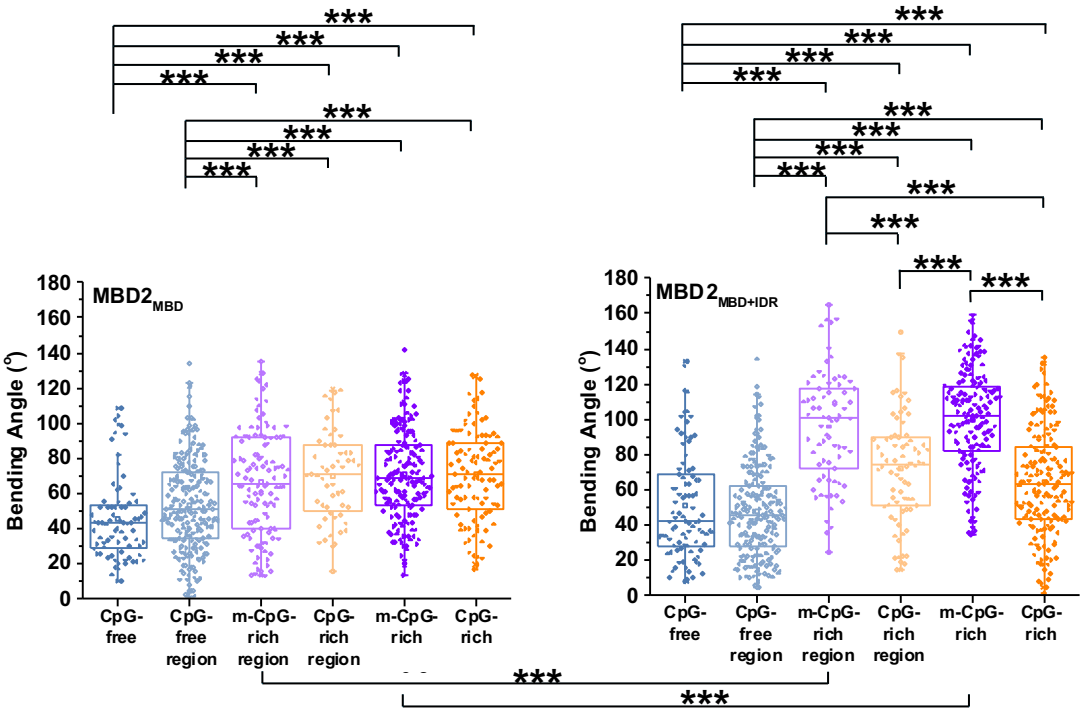

Supplementary Figure S9. Comparison of the DNA bending angles induced by MBD2. Box plots show the bending angles induced by binding of $MBD2_{MBD+IDR}$ and $MBD2_{MBD}$ to unmethylated and methylated CpG-free and CpG-rich DNA as well as the CpG-free and -rich regions within the CpG-free-rich DNA substrate. ***p < 0.0005. Significance values larger than 0.02 are not shown.